

---

# Relation-Oriented: Toward Knowledge-Aligned Causal AI

Jia Li

Department of Computer Science, University of Minnesota

jiaxx213@umn.edu

Xiang Li

Department of Bioproducts and Biosystems Engineering, University of Minnesota

lix5000@umn.edu

## Abstract

In machine learning, we naturally apply an *Observation-Oriented* principle, in which observational variables preexist and set the stage for constructing relationships. While sufficient for traditional models, the integration of AI with big data exposes the *misalignment* between the observational models and our actual comprehension. Contrarily, humans shape cognitive entities defined by relationships, enabling us to formulate knowledge across temporal and hyper-dimensional spaces, rather than being confined to observational constructs. From an innovative *Relation-Oriented* perspective, this study examines the roots of this misalignment within our current modeling paradigm, illuminated by intuitive examples from computer vision and health informatics. We also introduce the *relation-defined representation* learning methodology as a practical implementation of *Relation-Oriented* modeling, supported by extensive experimental validation.

## 1 Introduction

Existing modeling methods predominantly premise that relationships are established based on observed entities, designated as model variables. This *Observation-Oriented* principle can be traced back to the 1890s Picard-Lindelof theorem, which utilizes timestamps on a *logical timeline* to depict the absolute temporal evolution of observational variables, intending to establish a unique solution within the observational space.

Today, Artificial Intelligence (AI) has displayed capabilities surpassing humans in learning observations that meet the i.i.d. assumption, such as image generation in computer vision. Despite these, AI may appear “unintelligent” in comprehending certain relations that humans find intuitive. For instance, AI-created personas on social media can have realistic faces but barely with the presence of hands, due to AI struggling with the complex structure, instead treating hands as arbitrary assortments of finger-like items.

Moreover, when inquiries turn to time evolution, the task of causal reasoning makes a significant challenge for AI, although it is innate for humans. While traditional causal learning methods have made valuable contributions to numerous knowledge domains over the years Wood & Spekkens (2015); Vuković & Thalmann (2022); Ombadi et al. (2020), they are often challenged by a lack of generalizability Scholkopf et al. (2021). Specifically, these methods tend to be context-specific and struggle to generalize across diverse scenarios. In contrast to AI’s impressive achievements in areas such as Go gaming and natural language processing, its application to causality remains considerably constrained.

The questions “how to apply deep learning in causality” and “how to simulate hands” may seemly pertain to specific research domains such as causal inference and computer vision. However, they fundamentally converge towards the central issue of **AI Alignment**. Recalling Dr. Geoffrey Hinton’s caution, misalignment of AI capabilities with human values can lead to unintended detrimental consequences. Accordingly, the crux of the matter is, indeed “why causal knowledge and some time-irrelative relationships are unseen to AI? And how should we instruct it?” - an aspect that is increasingly critical to address.

Our knowledge initially starts from observations, yet our comprehension can surpass the observable reality, and construct knowledge to be *hierarchy* within a hyper-dimension, which is *unobservable* to AI. Such

hierarchy denotes granularity levels of phenomena in our comprehension. For instance, understanding individual traits (a higher individual level) relies on getting their cultural context (a lower population level). As highlighted by Scholkopf et al. (2021), for models to be generalizable, the low-level relations they learn must be reusable in subsequent high-level learnings.

In purely observational learning, the complications due to unobservable hierarchies can be directly illustrated in scenarios like the “unrealistic hands” problem (see Section 2.1). However, when we engage with causality, entailing a hierarchy of *dynamical* features within the *temporal* dimension, the ensuing complexities are greatly magnified. Intriguingly, the dynamics along a timeline can be viewed as *nonlinear* relationships (see Section 4.2); yet, in spite of neural networks’ inherent proficiency in handling nonlinearity, the latent potential of our current *Observation-Oriented* AI systems on the temporal dimension seems largely underutilized.

Contrary to AI, human understanding is fundamentally *relation-centric*. Relationships serve as indices that point to our mental representations Pitt (2022), shaping our cognitive understanding of observations and temporal events. Through relationships, we can form interconnected knowledge systems in memory. It’s not surprising that the cutting-edge methodology to teach AI causal reasoning focuses on “causal representations” Scholkopf et al. (2021), which is, letting the modeled objects represent the causal relations, instead of the observations. This concept indeed provides valuable insight into the pursuit of AI alignment.

Following a similar train of thought, we propose the **Relation-Oriented** principle, and a corresponding implementation method of *relation-defined representation* learning, which we consider an indispensable tool in our pursuit of knowledge-aligned AI. Sections 2 and 4 thoroughly examine our encountered challenges posed by: **1)** the unobservable knowledge hierarchy, and **2)** relationship across *multi-timelines* in such hierarchies, both neglected in our *Observation-Oriented* convention. In Section 3, we reassess existing causality methods, which inherently in a *Relation-Oriented* view but come with substantial limitations. Section 5 formally factorizes the process of relation-defined hierarchical representation, followed by Section 6, which outlines the proposed implementation methodology, subsequently validated by experiments detailed in Section 7.

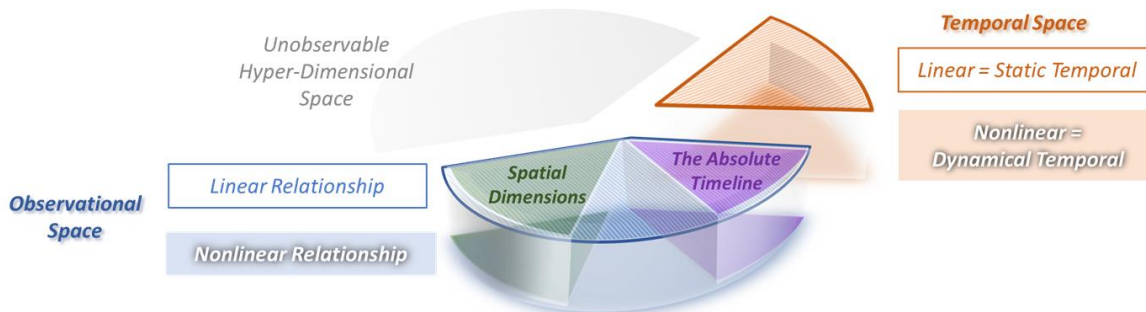


Figure 1: Differentiation among *Observational*, *Temporal*, and *Hyper-Dimensional* spaces, with the former two composing *Observable* space and the latter remaining *Unobservable*. For an in-depth discussion on the concept of temporal space and the absolute timeline, please see Section 4.

Figure 1 clarifies the terminologies concerning spaces and dimensions, with the hyper-dimension consisting of all the unobservable hierarchies in our knowledge. Within *Observable* space, relationships that connect distributions broadly fall into two categories: linear and nonlinear. The term “features” denotes potential variables that can represent the distributions of interest.

Typically, AI excels in addressing nonlinearity, while conventional models are adept at linear interpretation. However, in the temporal dimension, related nonlinear dynamics may span across *multiple logical timelines*. Frequently overlooked, this aspect can lead to *inherent temporal biases* in our models - Which narrow our successful AI applications within *observational* space only, and also obstruct causal learning from achieving generalizable success in *observational-temporal* space.

Contrarily, relation-defined representation aligns with knowledge definition, through which, AI can automatically identify the intended dynamics within the corresponding knowledge level. Our methodology’s feasibility rests on autoencoders, enabling a transition from the *observational-temporal* space to the latent feature space, which allows us to represent *dynamical* features in the same manner as *observational* ones.

## 2 The Unobservable Hierarchy in Knowledge

Knowledge hierarchies are inherent across many fields. Take flood prediction: general physical rules formulate the base-level regulations, applicable universally, while unique hydrological conditions create distinct watershed features. This paradigm applies to diverse phenomena like epidemic progression, economic fluctuations, or strategic decision-making, wherein knowledge extends from broad frameworks to specific idiosyncrasies.

In this section, we explore the knowledge hierarchies over observational and temporal features, via two illustrative examples. The first, grounded in computer vision, underlines how the direct challenges encountered in observational space learning are linked to the unobservable knowledge hierarchy. While the second, from health informatics, demonstrates how traditional causal learning typically only captures static temporal features, overlooking the intrinsic dynamical aspects of causality and their inherent hierarchies.

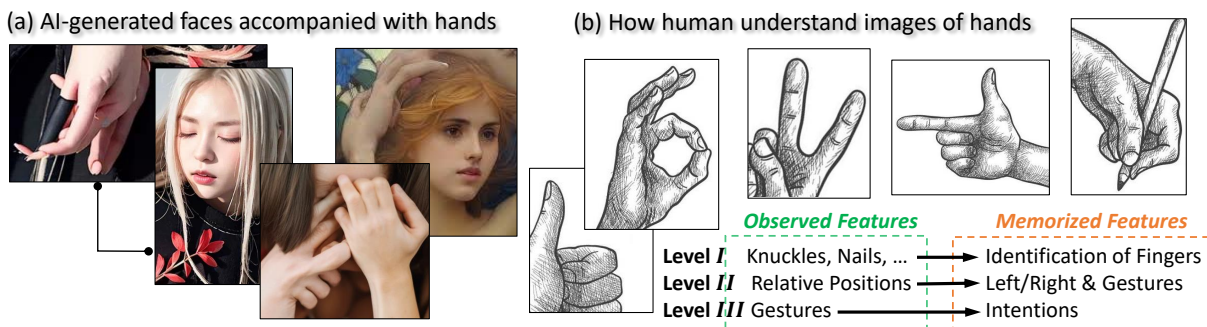


Figure 2: A comparison of AI-generated and human-sketched hand images. AI processes observed features simultaneously, thus treating hands as arbitrary mixtures of finger-like items. For humans, the process is hierarchical, where higher-level recognition relies on lower-level conclusions, even with incomplete views.

(c) Prior knowledge is encoded as an indicator function to connect specified features

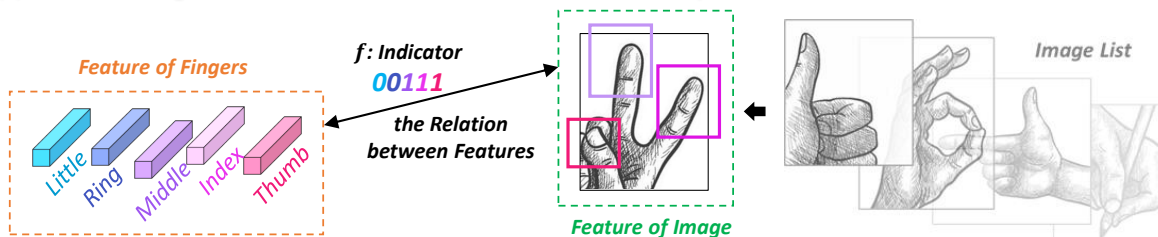


Figure 3: Traditional *Observation-Oriented* decomposition of the relationship in Level I knowledge.

### 2.1 Hierarchy of Observational Features

Figure 2(a) showcases AI-created realistic faces with unusual hands, while humans can easily distinguish a plausible hand and infer the owner’s intention, even in colorless pencil sketches, as in (b). We can quickly decompose observations into hierarchical features, progressing from lower to higher levels: **I**, knuckles, nails, and relative lengths identify fingers; **II**, their positions indicate a hand gesture; **III**, the gesture’s meaning is retrieved from memory. Unlike humans, AI systems process all observational features simultaneously, where the intuitive hierarchy in our understanding is unobservable from their perspective. Similarly, to an extraterrestrial, the unrealistic hands in Figure 2(a) may seem as normal as in actual hand photos.

However, without seeing the hierarchy, the hierarchical features may be revealed as distinguishable, if *no significant overlaps*. For instance, the placement of human eyes informs facial angle, allowing AI to generate plausible faces without recognizing “eyes” from “faces”. On the contrary, some different hand gestures might look similar. Without identification of “fingers” (Level I knowledge), AI may not recognize their varying positions (Level II knowledge) but misinterpret “hands” as arbitrary finger-like items associations.

This hierarchical organization of our comprehension enables us to effectively reuse knowledge across a range of scenarios. For instance, the finger identification (Level I knowledge) is transferable across photos, watercolor

paintings, and any sketching styles. As knowledge is accrued over time, the intra-level connections are strengthened, making our understanding of hierarchies more distinct and concrete. The relationship at each level can naturally form graphical models, where the connected features serve as nodes and readily interact with others in our cognition.

The leading technology for disentangling features, Variational AutoEncoders (VAEs) Burgess et al. (2018), are not designed to capture intra-level relations, but primarily to disentangle same-level features under i.i.d setting. This nature inherently limits VAEs to handling knowledge hierarchy. For instance, while VAEs can effectively disentangle the finger-level features, as shown on the left side of Figure 3, if the disentanglement is trained on data like watercolor paintings, they may struggle to recognize pencil sketches on the right side.

In traditional *Observation-Oriented* graphical modeling, a prerequisite often involves fully observed variables to establish relation functions, such as the indicator function  $f$  presented in Figure 3. This requires extensive manual labeling, which may not always be practical. Conversely, our proposed *Relation-Oriented* modeling emphasizes knowledge-based relations to construct observational representations inversely. Here,  $f$  is not a predetermined indicator, but an index of specifying features from the complex observations. Considering the data flow from left to right in Figure 3, a relation-defined  $f$  serves as a filter, to efficiently exclude color-related aspects from the VAE-captured representations, keeping only relevant data for the right side.

## 2.2 Hierarchy of Dynamical Temporal Features

A *reinforcement learning*-based AI system Sutton & Barto (2018) can potentially manage knowledge hierarchies in observational space with continuous human feedback. For example, it could learn to identify fingers autonomously, driven by human approval of images featuring typical five-fingered hands. However, spontaneous adjustments on the temporal dimension remain challenging. Before probing its intricacies, let’s examine hierarchical dynamics along a single timeline through the lens of traditional causal learning.

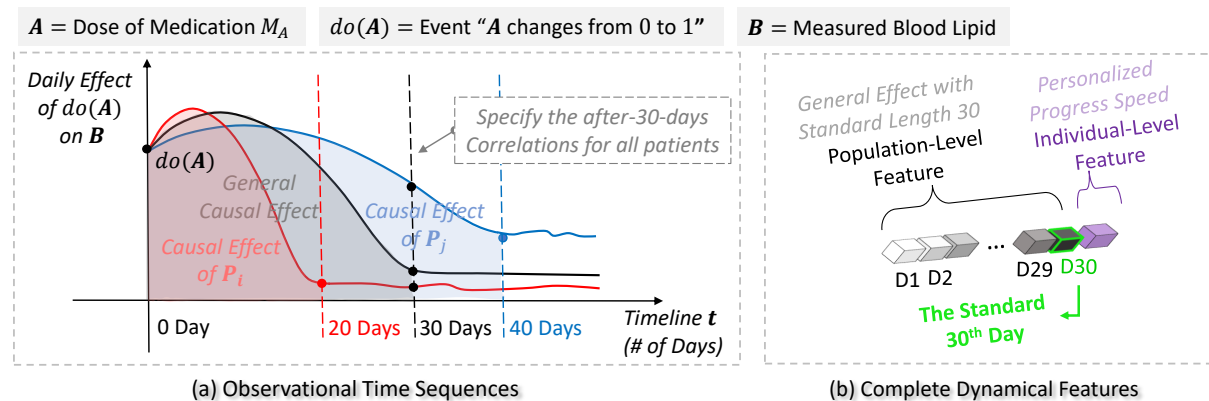


Figure 4: A hierarchical dynamics example. Medication  $M_A$  treats high cholesterol (i.e., blood lipid) with  $do(A)$  denoting its initial use. The population-level effect typically takes about 30 days to fully manifest (i.e., reaching the elbow at  $t = 30$ ), depicted by the black curve in (a). A younger patient  $P_i$  achieves this effect in 20 days, while an older patient  $P_j$  takes 40 days. Estimating the medical effect should consider their effects defined by the personalized elbows, but usually derived from their after-30-days correlations.

Figure 4(a) depicts the daily effects on patients following the initiation of medication  $M_A$  (i.e.,  $do(A)$ ), with  $t$  indicating the elapsed days. This classic causal relationship sees  $do(A)$  as the cause, and the time sequence on the  $t$ -axis reflects the ensuing effect. Assuming each patient’s (unobserved) personal characteristics linearly influence the medication’s release - uniformly accelerating or decelerating its progress - the observed time sequence for an individual (like the red and blue curves in (a)) is shaped by two levels of *dynamical* features: **1**) the population-level effect sequence with a standard length, and **2**) the individual-level progress speed.  $M_A$ ’s clinical effectiveness should be evaluated primarily based on level **1**), regardless of level **2**).

Figure 4(b) completely represents the dynamical features in a 31-length vector, segmented as two hierarchical levels. Traditional medical effect estimation, often obtained by averaging patients’ after-30-days

performances, essentially builds a correlation model  $B_{t+30} = f(do(A_t))$ . It only captures the final step of the standard effect sequence, disregarding the preceding 29 steps, thus only representing a *static* fragment of the population-level dynamic. Moreover, it implicitly assumes a normal distribution of patients’ personalized time spans around the mean value of 30 days with a linearly decreasing medical effect.

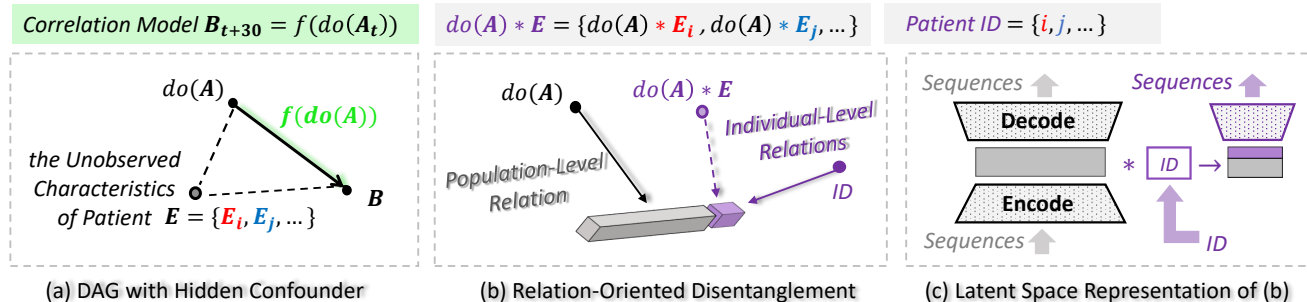


Figure 5: (a) The traditional causal inference. (b) Hierarchical disentanglement of dynamics using relations as indices. (c) Autoencoder-based generalized and individualized reconstructions of time sequences.

### 2.3 The Elusive Hidden Confounder

For individuals like  $P_i$  or  $P_j$ , the average effect estimated by model  $f$  introduces a bias:  $P_i$  exceeds 100% of the expected effect after 30 days, while  $P_j$  only achieves about 75%. To account for these individual-level biases, traditional causal DAG (Directed Acyclic Graph) introduces a *hidden confounder* (denoted as  $E$ ), to represent patients’ unobserved personal characteristics, as shown in Figure 5 (a). However, it raises a question - why concern ourselves with a hidden variable outside our model’s scope? This inclusion suggests an illogical assertion: “Our model is biased due to ignorance of some aspects we have no intent to investigate.”

The reason for introducing  $E$  is that while this common cause remains unknown, its effect - the individual-level dynamical speeds - is observable. Since such a level is overlooked by the traditional model  $f$ , it can only be attributed to the potentially existent  $E$ . Although hidden,  $E$  still represents an observational variable and thus could be incorporated by  $f$  once revealed. In essence, the introduction of this elusive hidden confounder is to transform *observed temporal* variables into *unobserved observational* ones. This serves to enhance human understanding, though does not necessarily benefit the model.

Figure 5(b) presents the hierarchical disentanglement of the dynamical features indexed by relations. Traditional causal inference views the individual-level effect as caused by the unobserved composite cause  $do(A)*E$ , which is an interpretable causal relationship, but not directly modelable. Conversely, a *Relation-Oriented* approach treats the relation merely as an index without requiring modeling. Thus, we can use any observed identifier, such as patient ID, to pinpoint the individual-level dynamics. Figure 5(c) illustrates the implementation architecture of this *Relation-Oriented* approach, showing two separate reconstruction processes of the time sequences data, with and without individual-level dynamical features, respectively.

## 3 Causality on the Timeline

Causality research can be seen as our probe into the temporal dimension, extending beyond the observational reality. Curiously, one might find it rare to see “incorporation of time” defined as the distinctive factor between causality and mere correlation in causal inference theories. While, as in our modeling context, instead of a philosophical one, what significance does this distinction hold?

To model time series, we frequently involve a timestamp dimension, to logically reflect the absolute time evolution in reality. For the model, however, this approach renders the line between causality and correlation indistinct, as it operates within our defined modeling space, irrespective of temporal significance. Yet, this does not diminish the importance of the temporal dimension. Quite the contrary, reliance on the single absolute timeline has obstructed our accurate understanding of the temporal dimension’s role within the modeling context. In this section, we will discuss causal modeling from this perspective.

---

### 3.1 Causality vs. Correlation

Consider a general model function  $Y = f(X; \theta)$ , with  $\theta$  denoting the model parameter. The learning process for  $\theta$  is independent of how we interpret the  $X \rightarrow Y$  relationship, instead, relying solely on the observations of variable  $X$  and outcome  $Y$ . It is essential to recognize that a causal relationship comprises two layers: **1)** the basic connection that can be handled by models, and **2)** the interpretative information or constraints that are determined by us, such as the intentional causal directionality.

For example, to model causality  $X \rightarrow Y$ , the function  $Y = f(X; \theta)$  can be interpreted as predicting the effect on  $Y$ , while  $X = g(Y, \psi)$  can be viewed as a reverse inference for the cause  $X$ . However, irrespective of the modeling direction, parameters  $\theta$  and  $\psi$  consistently derive from the joint probability  $\mathbf{P}(X, Y)$ . Thus, the modeling perspective remains unaltered, regardless of the direction of causality.

The driving force behind identifying causal directions primarily stems from the risks of losing the dynamical features of the effect, rather than their logical differences. For example, in Figure 5(a), the correlation model  $f$  ignores the individual-level dynamical feature and necessitates the inclusion of a hidden confounder to inform our prior understanding. In other words, if the temporal features, including the hierarchically structured dynamical ones, can be fully represented by variables, a causal relationship can be viewed as a basic connection, like a mere correlation, with extra features added to record its causally significant direction.

**Lemma 1.** Causality vs. Correlation in the modeling context.

- Causality is connection between variables, which can be *observational*, *temporal*, and also *dynamical*.
- Correlation is connection between variables, which are *not dynamical*.

In short, the distinction between causality and correlation lies in the features connected in this relationship, instead of the connection (see Section 4.2 for examples). To use an analogy, a double-ended cotton swab is differentiated by the characteristics of its cotton ends - such as shape, texture, or color for different uses - rather than the connecting stick. For traditional models, due to the limitation in capturing hierarchical dynamics, a causal relationship has to be discerned for further manual interpretations.

Besides, there exists a common misconception about the distinction - The presence of a time lag between the cause event and its effect is often considered to signify this scenario as causal. We employ an example below to underscore it is not the defining factor in determining causality in the modeling context.

Morgan Spurlock conducts a self-experiment in the documentary film “Super Size Me” (2004). Over a month, Spurlock restricted his diet solely to McDonald’s meals, during which he recorded significant deteriorations in his health and physical appearance, including rapid weight gain, mood instability, liver damage, etc., which dramatically demonstrated the potential negative health impacts of a fast-food diet. Consider two time sequences:  $\mathbf{x} = \{x_1, \dots, x_{30}\}$  and  $\mathbf{y} = \{y_1, \dots, y_{30}\}$ . Here, each  $x_t$  signifies the act of eating McDonald’s on the  $t$ -th day, while each  $y_t$  corresponds to the fluctuations in his health indices for that particular day. It is intuitive to recognize that  $\mathbf{x} \rightarrow \mathbf{y}$  is a causal relationship, although no time lag exists between  $\mathbf{x}$  and  $\mathbf{y}$ . Yet, a time lag is also conceivable in this case. Suppose another person tried this experiment, but since he had a longer responding digestive system, the same effect denoted by  $\mathbf{y}$  emerged with a 5-day delay, creating a 5-day lag between  $x_1$  and  $y_1$ . This instance underlines that whether the time sequential cause and effect are separated by a time difference is not a reliable criterion to identify a causal model.

### 3.2 Current Causal Modeling Context

Figure 6 broadly classifies causal queries into four categories, based on the integration of temporal features and the necessity of discovering unknown relationships. The rectangle signifies all relationships with causal significance, while the blue circle identifies the potentially modelable scope. The current causal modeling is viewed from two aspects on the right side: the modeled *connection* that regards the relation capturing, and modeled *direction* that regards its potential causal interpretation.

(1) Aspect of the Basic Connection

The traditional causal inference has made notable advancements in exploring the specific conditions under which dynamical features can be partially “downgraded” to a level accessible by the employed statistical models. Notably, *do-calculus* probes into identifiable events (i.e., manually identifying dynamics as entities) to form temporal dimension variables Pearl (2012), but falls short in identifying dynamics of effects (refer to 4.2 for analysis). For these overlooked effect dynamics, if existing knowledge can suggest potential causes, the creation of a *hidden confounder* (see Section 2.3) can enhance comprehension; if not, these dynamics may be dismissed based on the *causal sufficiency assumption*, which could lead to subsequent challenges.

On the other hand, causal discovery methods mainly scan the observational space, possibly capturing static temporal features. As a result, if the causal mechanism does not encompass crucial dynamics, causal discovery can be effective. However, if such dynamics exist, they largely go undetected. This potential gap can be negated under the *causal faithfulness assumption* that observed variables fully represent the causal reality.

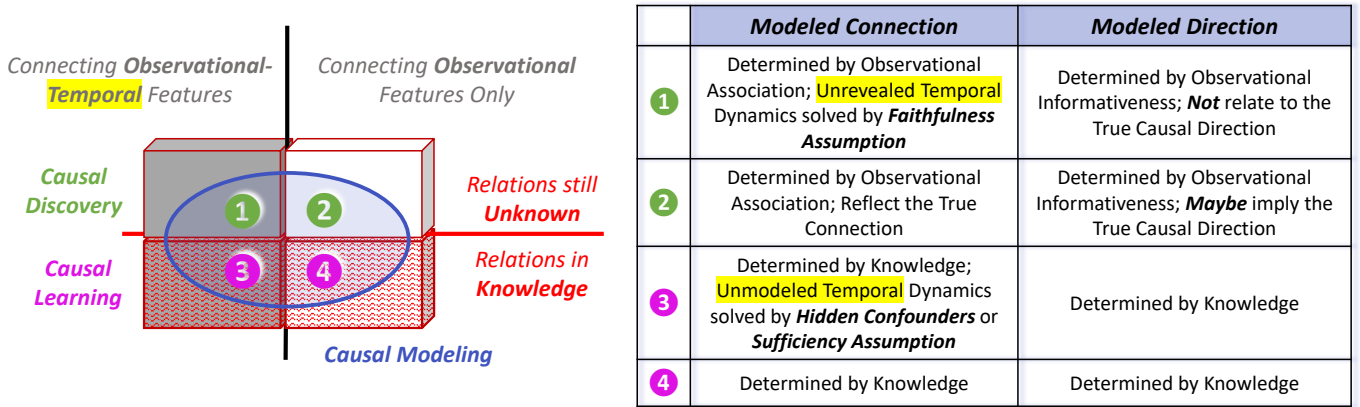


Figure 6: The Current Causal Modeling Context.

(2) Aspect of the Causal Direction

Consider observables  $X$  and  $Y$  in a graphical system, with specified models  $Y = f(X; \theta)$  and  $X = g(Y; \psi)$ . Based on observations, the discovered causal direction between  $X$  and  $Y$  is determined by the likelihoods of estimated parameters  $\hat{\theta}$  and  $\hat{\psi}$ . Given the joint distribution  $\mathbf{P}(X, Y)$ , one would prefer  $X \rightarrow Y$  if  $\mathcal{L}(\hat{\theta}) > \mathcal{L}(\hat{\psi})$ . Now, let  $\mathcal{I}(\theta)$  be a simplified form of  $\mathcal{I}_{X,Y}(\theta)$ , the Fisher information representing the amount of information contained by  $\mathbf{P}(X, Y)$  about unknown  $\theta$ . Assume  $p(\cdot)$  to be the probability density function; then, in this context,  $\int_X p(x; \theta) dx$  remains constant. So, we have

$$\begin{aligned} \mathcal{I}(\theta) &= \mathbb{E}[(\frac{\partial}{\partial \theta} \log p(X, Y; \theta))^2 | \theta] = \int_Y \int_X (\frac{\partial}{\partial \theta} \log p(x, y; \theta))^2 p(x, y; \theta) dx dy \\ &= \alpha \int_Y (\frac{\partial}{\partial \theta} \log p(y; x, \theta))^2 p(y; x, \theta) dy + \beta = \alpha \mathcal{I}_{Y|X}(\theta) + \beta, \text{ with } \alpha, \beta \text{ constants.} \end{aligned}$$

$$\text{Thus, } \hat{\theta} = \arg \max_{\theta} \mathbf{P}(Y | X, \theta) = \arg \min_{\theta} \mathcal{I}_{Y|X}(\theta) = \arg \min_{\theta} \mathcal{I}(\theta), \text{ and } \mathcal{L}(\hat{\theta}) \propto 1/\mathcal{I}(\hat{\theta}).$$

Subsequently, the likelihoods of the estimated parameters  $\hat{\theta}$  and  $\hat{\psi}$  depend on the amount of information,  $\mathcal{I}(\hat{\theta})$  and  $\mathcal{I}(\hat{\psi})$ . Thus, the directionality learned among variables essentially indicates how much their specified distributions are reflected in the data, with the more dominant one deemed the “cause”. This interpretation assumes that the cause must be more thoroughly represented in observations than the effect.

In summary, a causal direction inferred from observations could be causally meaningful if: **1)** the causality of interest does not involve significant dynamics, **2)** the observations are known, a prior, to be more informative about the cause than the effect, and **3)** the specified distributions are fundamentally accurate. Strictly speaking, the traditional “causal model” does not denote technically specified models, but those necessitating supplementary causal interpretations to fill our comprehension gaps and enable potential improvement.

---

## 4 The Overlooked Temporal Dimensionality

We often store data in matrices, with time series data incorporating an extra attribute for the timestamps, which forms a logical timeline, reflecting the absolute timeline in reality. Accordingly, when modeling, we used to rely on this singular timeline to define the chronological order of all potential events. However, our innate understanding of time is far more intricate and cannot be reduced to a single absolute timeline.

Consider an analogy where ants dwell on a two-dimensional plane of a floor. If these ants were to construct models, they might use the nearest tree as a reference to specify the elevation in their two-dimensional models. By modeling, they observe an increased disruption at the tree’s mid-level, which indicates a higher chance of encountering children. However, since they fail to comprehend humans as three-dimensional beings, instead of interpreting this phenomenon in a new dimension “height”, they solely relate it to the tree’s mid-level. If they migrate to a different tree with a varying height, where mid-level no longer presents a risk, they might conclude that human behavior is too complex to model effectively. Similarly, when modeling time series, we usually discount the dimension “time” as the single absolute timeline, which has become our “tree”.

Our understanding allows for the simultaneous existence of multiple logical timelines. If one is designated as the absolute timeline, the remaining ones can be viewed as relative timelines, each representing distinctive temporal events interconnected via specific relationships. In such *Relation-Oriented* perspective, e.g., during a causal inference analysis, the temporal dimension could incorporate numerous possible logical timelines that we could choose to construct any necessary scenarios. However, once we enter a modeling context, e.g., using AI to model the time series along a single absolute timeline, the temporal dimension no longer exists, but only a regular dimension containing timestamps, indistinguishable from other observational values. Metaphorically, if we consider the observational space for AI modeling as Schrödinger’s box and our interest is the “cat” within, our task is to accurately construct the box, giving adequate consideration to all potential logical timelines, to ensure the “cat” remains *reasonable* upon unveiling.

**Lemma 2.** *Temporal Dimension* refers to the aggregation of all potential logical timelines, not a single one. A *Temporal Space* in comprehension is the space built by chosen timelines as axes.

Fundamentally, as three-dimensional beings, we are limited from truly understanding temporal dimensionality. As the term “space” typically evokes a three-dimensional conception, the notion of “temporal space” might seem odd for a four-dimensional creature. Like ants can use trees as references without the need to fully comprehend the third dimension, we rely on logical timelines to interpret the fourth. At this juncture, our mission is to recognize the potential “forest” beyond the present single “tree”.

In this section, we will initially dissect the mechanism of inherent temporal bias, due to neglecting potential multi-timelines; then, reassess existing methods of learning dynamics; and last, summarize advancements and challenges on our journey towards realizing knowledge-aligned causal AI.

### 4.1 Inherent Temporal Bias

Overlooking multi-timelines in *structural causal models* (SCMs) can lead to *inherent temporal biases*. These biases substantially limit our ability to fully harness AI’s potential in modeling nonlinear dynamics, especially within some large-scale causal relationships that may include more complex hidden timelines.

To better ascribe this issue, we *redefine* the causal Directed Acyclic Graph (DAG) Pearl (2009) as follows: **1**) incorporating (potentially multiple) logical timelines as axes into the DAG space, and **2**) defining edges along timeline axes to be vectors with meaningful lengths indicating the timespans of causal effects. For example, the single-timeline scenario in Figure 4 has the redefined DAG depicted in Figure 7(b), with (a) showing the traditional one as a comparison. The edge  $do(A) \rightarrow B$  in Figure 7(a) can only (partially) represent population-level effect, thus necessitates a hidden confounder to explain the individual-level diversities, while in Figure 7(b), they can be explicitly represented by varying lengths of  $\overrightarrow{do(A)} \overrightarrow{B}$ .

Consider an expanded two-timeline scenario in Figure 8(a), where  $A$  shorthandly represents  $do(A)$ . Apart from its primary effect on  $B$ ,  $A$  also indirectly influences  $B$  through its side effect on another vital sign,  $C$ ,

depicted as edges  $\overrightarrow{AC}$  and  $\overrightarrow{CB}$ . For simplicity, assume the timespan for  $\overrightarrow{AC}$  is 10 days for all patients, with the individual-level diversity solely confined to timeline  $T_X$ . In conventional single-timeline causal modeling, the SCM function would be  $B_{t+30} = f(A_t, C_{t+10})$ . Let's assume  $f(A_t, C_{t+10})$  is implemented using RNNs, which could accurately depict the individual-level final effects of  $A$  on  $B$  for any patient.

The confounding relationship over nodes  $\{A, B, C\}$  forms a triangle across timelines  $T_X$  and  $T_Y$  - such shape geometrically holds for any hierarchical level relationship. For patients  $P_i$  and  $P_j$ , the *individualization* process is to “stretch” this triangle along  $T_X$  by different ratios, which is a homographic *linear transformation* in this space. However, as illustrated in Figure 8 (b) and (c), for either  $P_i$  or  $P_j$ , equating the outcome of  $f$  to be  $B_{t+30}$  violates the *causal Markov condition* necessary for reasonable SCMs.

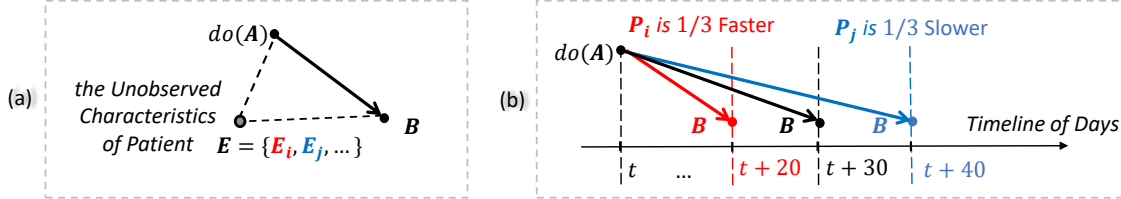


Figure 7: (a) Traditional Causal DAG introducing hidden  $E$ . (b) Redefined DAG: the standard black vector signifies the population-level effect, while the individual-level ones are represented by its different scaling.

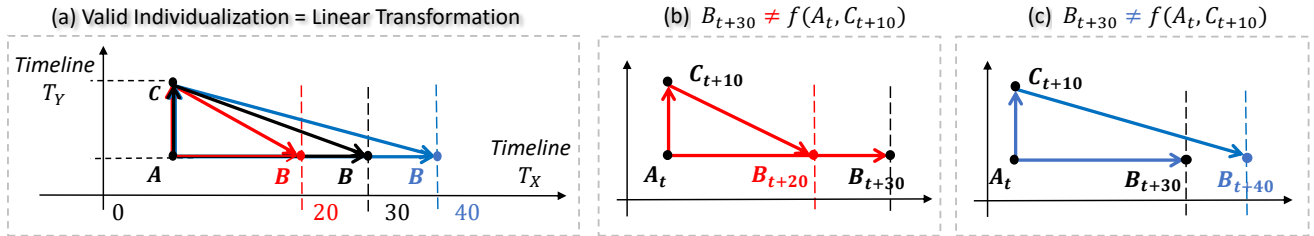


Figure 8: (a) A two-timeline (redefined) DAG space, where a valid individualization presents a linear transformation. (b)(c) Violations of the Markov condition for the prevailing SCM with confounding across timelines.

Notably, in this specific case, the violation may not cause significant issues for RNN models. Given the independence of dynamical features on  $T_X$  and  $T_Y$ , the SCM can be formulated as  $B_{t+30} = f_1(A_t) + f_2(C_{t+10})$ . This suggests that the cross-timeline confounding can be broken down into two single-timeline issues, where capturing hierarchical dynamics might challenge statistical models but not RNNs. However, assuming special conditions like independence or non-confounding is impractical. Given that each pair of cause and effect could potentially inhabit a logical timeline, such temporal biases are inherently prone to exponentially accumulate and influence our SCM applications, regardless of the model chosen.

**Lemma 3.** The traditional SCM may have the inherent temporal bias if containing: **1)** *Confounding* of dynamics across *Multiple* logical timelines, and **2)** Unobservable hierarchy of such confounding.

It is interesting to notice that most of the successful applications instinctively avoid one of the two factors: *confounding* or *multi-timelines*. For statistical causal models, the interpretability allows them to be manually adjusted to facilitate de-confounding, e.g., the backdoor adjustment Pearl (2009). For AI models, most of the sweeping achievements do not potentially involve relative timelines, e.g., the large language model (LLM) in a semantic space, where the phrases are ordered consistently along a single logical timeline.

Unlike AI's black-box nature, causal inference inherently takes a *Relation-Oriented* view. But in its context, the inherent temporal biases are difficult to identify, as they often intermingle with biases resulting from the inability to model nonlinearity - They similarly manifest as statistical diversity (or data heterogeneity) among levels, and both can be addressed via de-confounding. Consider Figure 7(a), a correlation model that only captures the population-level effect can mismatch with individuals  $P_i$  and  $P_j$ , which may not be distinguishable from the model mismatching in Figure 8(b)(c), caused by crossing two timelines.

## 4.2 Learning Dynamics

For observational variable instance  $x \in \mathbb{R}^d$ , we frequently encode its temporal evolution as sequential timestamps along a timeline, such as  $\{x_t\} = \{x_1, \dots, x_t, x_{t+1}, \dots, x_T\}$ , without considering  $t$  as a separate dimension. Accordingly, we seldom view  $x$ 's changing value over time as a "distribution" along the  $t$ -axis. When making predictions like  $x_{t+m} = f(x_t)$ , the potential nonlinearity of function  $f$  is only acknowledged within  $\mathbb{R}^d$ , but leaving the relationship between  $x_t$  and  $x_{t+m}$  to be *linear*. It implies that the **correlation** model  $x_{t+m} = f(x_t)$  can only capture the **static** temporal features of  $\{x_t\}$ . If, however, no suitable  $(f, m)$  can be found to ensure this model adequately represents the temporal distribution of  $\{x_t\}$ , there may exist unrepresented **dynamical** temporal features. This necessitates a **causality** function of the general form  $\{y_\tau\} = f(\{x_t\})$ , with cause and effect represented as two distinct sequences on logical timelines,  $\tau$  and  $t$ , respectively. Therefore, the relationship between any pair of  $x_t$  and  $y_\tau$  could be *nonlinear*.

Causal models for time series often take the form  $y_\tau = f(\{x_t\})$  with  $\tau = (t + T) + m$ , representing a sequence on timeline  $t$  causing a static outcome (or a sequence of length one),  $m$  timesteps later on  $t$ . Examples include autoregressive models Hyvärinen et al. (2010) and RNNs Xu et al. (2020). The *linearity* of function  $f$  with respect to  $T$  elements of  $\{x_t\}$  will restrict models to a **single-level dynamic**. For instance, in Figure 4(b), using 30 correlation models for 30 days can capture the population-level sequence but still neglect individual-level speeds. Contrarily, RNNs embrace nonlinearity and potentially can capture both levels, although without ensured disentanglement.

Models like RNNs primarily target dynamics of cause, rendering the effect to be static. We can designate potential significant time sequences for the cause, but pinpointing precise start and end timestamps for the ensuing effect remains challenging. The Granger causality model Maziarz (2015), widely used in economics, employs the general causality function form  $\{y_\tau\} = f(\{x_t\})$ , where  $t$  and  $\tau$  are distinct timelines, acknowledging the existence of possible *multi-timelines*. However, as a statistical test model, it primarily handles single-level linear changes and necessitates sequence specifications for both cause and effect.

A more universally applicable concept of dynamics is the *do-calculus* Pearl (2012); Huang & Valtorta (2012), which refrains from assuming specific sequences. Instead, it treats *identifiable* temporal events as objects around which it conducts elementary calculus, adopting a more *Relation-Oriented* viewpoint. In the subsequent discussion, we will revisit the three rules of *do-calculus* from a differential-and-integral perspective. For sequence  $\{x_t\} = \{x_1, \dots, x_T\}$ , we denote  $do(x_t) = \{x_t, x_{t+1}\}$  to indicate the occurrence of an instantaneous event  $do(x)$  at time  $t$ . The time lag  $\Delta t$  between  $\{t, t + 1\}$  is assumed to be sufficiently small to make this event elementary, allowing the *interventional* effect of  $do(x_t)$  to be represented as a function of the resultant distribution at  $t + 1$ . Conversely, the effect provoked by a static  $x_t$  is an *observational* effect. Therefore, as the cause, dynamics of variable  $X \in \mathbb{R}^d$  over a period of length  $T$  can be formulated as:

Given  $\mathcal{X} \rightarrow Y \mid Z$ , where  $\mathcal{X} = \langle X, t \rangle \in \mathbb{R}^{d+1}$  encompass sequence  $\{x_t\}$ , we have the cause

$$\mathcal{X} = \int_0^T do(x_t) \cdot x_t dt \quad \text{with} \quad \begin{cases} (do(x_t) = 1) \mid do(z_t), & \text{Observational only (Rule 1)} \\ (x_t = 1) \mid do(z_t), & \text{Interventional only (Rule 2)} \\ (do(x_t) = 0) \mid do(z_t), & \text{No interventional (Rule 3)} \\ \text{otherwise} & \text{Associated observational and interventional} \end{cases}$$

The effect of  $\mathcal{X}$  can be derived as  $f(\mathcal{X}) = \int_0^T f_t(do(x_t) \cdot x_t) dt = \sum_{t=0}^{T-1} (y_{t+1} - y_t) = y_T - y_0$

Fundamentally, the three rules of *do-calculus* address all conceivable conditional independencies between the *observational* and *interventional* effects within the  $\{X, Y, Z\}$  graphical system, sidestepping the most general cases. If the associated causes, denoted as  $do(x_t) \cdot x_t$ , can be specified, this scenario would align with Rule 2.

Given the substantial flexibility provided by the  $do(\cdot)$  format, we can also represent the effect  $Y$  dynamically, by introducing timeline  $\tau$  as an extra dimension, yielding  $\mathcal{Y} = \langle Y, \tau \rangle$ . Nonetheless, determining the *identifiable* events within  $\mathcal{Y}$  still necessitates manual specification, in contrast to our proposed relation-defined representation learning approach, which can construct  $\mathcal{Y}$  automatically.

### 4.3 Toward Knowledge-Aligned AI

Our quest for authentic AI, causally reasoning and aligned with our knowledge, involves broadening our modeling techniques from purely observational to include temporal and hyper-dimensional spaces. Referring to Figure 9, the present challenge hinges on harnessing the capabilities of AI within structural models for causal reasoning, with the crux residing in identifying potential relative timelines. Considering that both logical timelines and knowledge hierarchies remain unobservable directly, it becomes crucial for us to shift from an *Observation-Oriented* to a *Relation-Oriented* modeling paradigm.

Model	Principle	Cause	Connection & Direction	Effect	Handle Unobservable Hierarchy	Capture Dynamics
<i>Mechanistic or Physical</i>	$Y = f(X; \theta)$	Observational-Temporal $\langle X, t \rangle$	by Knowledge	Observational-Temporal $\langle Y, t \rangle$	Yes	Yes
<i>Relation-Oriented Structural Model</i>	Given $P(X, Y)$ & $X \rightarrow Y$	Observational-Temporal $\langle X, t \rangle$	Learn Representation $\hat{Y} = f(X; \theta)$	Observational-Temporal $\langle \hat{Y}, t \rangle$	Yes	Yes
<i>Structural Causal Learning</i>	Given $P(X, Y)$ & $X \rightarrow Y$ $Y = f(X; \theta)$	Observational $X$ & Sequential $\{X_t\}$	Connected via $\theta$ $X \rightarrow Y$ by Knowledge	Observational & Static $Y_t$	?	?
<i>Graphical Causal Discovery</i>	Given $P(X, Y)$ Specify $\vartheta$ Find $L(Y X; \vartheta) > L(X Y; \vartheta)$	Observational $X$	Connected via $\vartheta$ $X \rightarrow Y$ by Observed Info	Observational $Y$	?	No
<i>Common Cause Model</i>	Given $P(X, Y Z)$	Observational $X$	Connected via $Z$	Observational $Y$	?	No
<i>i.i.d Data Driven Model</i>	Given $P(X, Y)$	Observational $X$	None	Observational $Y$	No	No

Figure 9: Simple Taxonomy of Models (Adapted in part of Table 1 in Scholkopf et al. (2021)), from more knowledge-driven (top in purple) to more data-driven (bottom in green). Notations:  $\vartheta$  = joint distribution,  $\theta$  = conditional distribution,  $\langle X, t \rangle$  = augment  $t$  as an additional dimension, “?” = depending on practice.

The initial models under i.i.d. assumption only approximate observational associations, proved unreliable for causal reasoning Pearl et al. (2000); Peters et al. (2017). Correspondingly, the common cause principle highlights the significance of the nontrivial conditional properties, to distinguish structural relationships from statistical dependencies Dawid (1979); Geiger & Pearl (1993), providing a basis for effectively uncovering the underlying structures in graphical models Peters et al. (2014).

Graphical models, employing conditional dependencies to construct Bayesian networks (BNs), often operate in observational space and neglect temporal aspects, reducing their causal relevance Scheines (1997). Notably, causally significant models, such as Structural Equation Models (SEMs) and Functional Causal Models (FCMs) Glymour et al. (2019); Elwert (2013), are equipped to address *counterfactual* queries Scholkopf et al. (2021) - We reinterpret as capturing *temporal distributions* and responding to *conditional* questions. Typically, these models leverage prior knowledge to construct causal Directed Acyclic Graphs (DAGs).

State-of-the-art deep learning applications on causality, which encode the DAG structural constraint into continuous optimization functions Zheng et al. (2018; 2020); Lachapelle et al. (2019), undoubtedly enable efficient solutions for large-scale problems. However, this approach potentially conceals numerous relative timelines, which may result in substantial temporal biases. This is particularly apparent in the limited success of applications that incorporate DAGs into network architectures Luo et al. (2020); Ma (2018), such as Neural Architecture Search (NAS). Schölkopf Scholkopf et al. (2021) succinctly highlights three key challenges impeding the broader success of causal AI: 1) limited model robustness, 2) insufficient model reusability, and 3) inability to handle heterogeneity. The first two challenges can be associated with inherent temporal biases, while the latter originates from the unobservable knowledge hierarchy.

On the flip side, physical models, which explicitly integrate the temporal dimension, able to establish abstract concepts through structural knowledge, may provide insights into our upcoming challenges. The proposed *Relation-Oriented* modeling is designed along these lines, aiming to transcend the observational limitations innate to our prevailing modeling paradigms.

## 5 Obs-Tmp Representations' Hierarchical Disentanglement

Let  $X \in \mathbb{R}^d$  denote an observational variable, with instance sequences in data presenting its dynamics. Suppose a logical timeline  $t$  exists, along which,  $X$ 's sequence can be denoted as  $\{x_t\} = \{x_1, \dots, x_t, x_{t+1}, \dots, x_T\}$ . We aim to devise a latent feature space  $\mathbb{R}^L$  for two purposes: **1)** Establish representation of the observational-temporal (obs-tmp) variable  $\mathcal{X} = \langle X, t \rangle \in \mathbb{R}^{d+1}$  in  $\mathbb{R}^L$ , fully capturing observational and dynamical features of the sequence  $\{x_t\}$  in data. **2)** Disentangle this representation in  $\mathbb{R}^L$  according to desired hierarchy.

Also, we want this hierarchical disentanglement to be indexed via relationships, reflecting different levels of knowledge. The advantage of this form is that the representations we establish, defined and encapsulated by recognized relations, are highly *reusable*, accommodating further structural modeling. Consequently, this method enables the *generalization* of the desired knowledge level across varied contexts.

Consider another observational variable  $Y \in \mathbb{R}^b$ , and suppose its dynamical sequence is along logical timeline  $\tau$ , denoted as  $\{y_\tau\}$ . Given relationship  $\mathcal{X} \rightarrow \mathcal{Y}$ , the proposed **relation-defined representation** learning is to establish representation of  $\hat{\mathcal{Y}} = \langle \hat{Y}, \tau \rangle \in \mathbb{R}^{b+1}$  in the latent space, which represents a new data sequence  $\{\hat{y}_\tau\}$ , versioned from  $\{y_\tau\}$  by selecting its observational-temporal features that can only be caused by  $\mathcal{X}$ .

In structural modeling, for example, the causal system  $\mathcal{X} \rightarrow \mathcal{Y} \leftarrow \mathcal{Z}$  can be disassembled into  $\mathcal{X} \rightarrow \hat{\mathcal{Y}}$  and  $\mathcal{Z} \rightarrow \tilde{\mathcal{Y}}$ , allowing flexible reuse of both  $\hat{\mathcal{Y}}$  and  $\tilde{\mathcal{Y}}$  representations. Furthermore, if consider  $\mathcal{Y}$  features a two-level hierarchy, with the first determined by  $\mathcal{X} \rightarrow \mathcal{Y}$  and the second by  $(\mathcal{X}, \mathcal{Z}) \rightarrow \mathcal{Y}$ , we can also establish the representation of  $\mathcal{Y}$  as hierarchically disentangled, where the second level builds upon the first, introducing an additional data stream from  $\mathcal{Z}$ .

Next, we will sequentially factorize three transformation processes between the data and latent space  $\mathbb{R}^L$ : First, observational features from  $\mathbb{R}^d$  to  $\mathbb{R}^L$ ; Second, observation-temporal features from  $\mathbb{R}^{d+1}$  to  $\mathbb{R}^L$ ; Last, the relationship  $\mathcal{X} \rightarrow \mathcal{Y}$ , from the joint space  $\mathbb{R}^{d+1} \circ \mathbb{R}^{b+1}$  to  $\mathbb{R}^L$ .

### 5.1 Factorization of Observational Hierarchy

Assume  $X = (X_1, \dots, X_d) \in \mathbb{R}^d$  exhibits an  $n$ -level hierarchy. We utilize  $\Theta_i$  to signify its  $i$ -th level observable feature in the data form, while its corresponding latent space feature is denoted as  $\theta_i$ . Then, we obtain:

$$X = \sum_{i=1}^n \Theta_i, \text{ where } \Theta_i = f_i(\theta_i; \Theta_1, \dots, \Theta_{i-1}) \text{ with } \Theta_i \in \mathbb{R}^d \text{ and } \theta_i \in \mathbb{R}^{L_i} \subseteq \mathbb{R}^L \quad (1)$$

In this context,  $\theta_i$  is considered as a vector in  $\mathbb{R}^L$ , in which only a subset of the  $L$  dimensions carries significant value, represented as the subspace  $\mathbb{R}^{L_i}$ . The hierarchical disentanglement is depicted by the arrangement of these subspaces:  $\{\mathbb{R}^{L_1}, \dots, \mathbb{R}^{L_i}, \dots, \mathbb{R}^{L_n}\}$ . Accordingly, the representation function  $f_i$  enables the  $i$ -th level transformation between  $\mathbb{R}^d$  and  $\mathbb{R}^{L_i}$ , drawing its potential attributes from all preceding lower-level features.

To illustrate this factorization, consider Figure 2 (b). Let's say  $\theta_1, \theta_2$ , and  $\theta_3$  effectively represent the features spanning from Level I to III, exclusively occupying meaningful subspaces  $\mathbb{R}^{L_1}, \mathbb{R}^{L_2}$ , and  $\mathbb{R}^{L_3}$ . The image can be fully represented as an augmented vector  $\langle \theta_1, \theta_2, \theta_3 \rangle \in \mathbb{R}^L$ . Correspondingly,  $\Theta_1, \Theta_2$ , and  $\Theta_3$  are full-sized images containing distinct content. Their cumulative representation can progressively render the complete image. E.g.,  $\Theta_1$  isolates the fingers' details, while  $\Theta_1 + \Theta_2$  broadens to depict the entire hand.

### 5.2 Factorization of Obs-Tmp Hierarchy

For the time sequence of  $X$ , denoted as  $\{X_t\} = \{X_t \in \mathbb{R}^d \mid t = 1, \dots, T\}$ , it can be viewed as a  $d$ -dimensional vector extending  $T$  times, while we aim to represent it in a new form  $\mathcal{X} = \langle X, t \rangle \in \mathbb{R}^{d+1}$  in  $\mathbb{R}^L$ , such that:

$$\mathcal{X} = \sum_{i=1}^n \Theta_i, \text{ where } \Theta_i = f_i(\theta_i; \Theta_1, \dots, \Theta_{i-1}) \text{ with } \Theta_i \in \mathbb{R}^{d+1} \text{ and } \theta_i \in \mathbb{R}^{L_i} \subseteq \mathbb{R}^L \quad (2)$$

It is essential to note that each  $\theta_i \in \mathbb{R}^{L_i}$  represents an observational-temporal feature, corresponding to the observable component  $\Theta_i \in \mathbb{R}^{d+1}$ . The latter can also be represented in its original time sequence

form  $\{\Theta_t\}_i = \{\Theta_{t_i} \in \mathbb{R}^d \mid t_i = 1, \dots, T\}$ . Hence, we have a collection of logical timelines  $\{t_1, \dots, t_i, \dots, t_n\}$ , relative to the *absolute* timeline  $t$  in this context. These  $n$  relative timelines, while may or may not be distinct, are each individually determined by their corresponding relationships. This allows each  $t_i$  to automatically adapt to the specifics of its associated relation, liberating us from recognizing potential timelines. For each level of observation, denoted by the summation  $\Theta_1 + \dots + \Theta_i$ , the presented form is consistently an observable time sequence along  $t$ , without concerns about inherent temporal biases.

Consider the scenario depicted in Figure 8, with data stored in a matrix comprising four columns: values of  $A$ ,  $B$ ,  $C$ , and timestamps  $t$ . We can represent  $B$  as a 2-level hierarchy: the first level is defined by its direct effect from  $A$  ( $A \rightarrow \hat{B}$ ), while the second level incorporates an additional stream denoting its indirect effect via  $C$  ( $A \rightarrow C \rightarrow \tilde{B}$ ). The comprehensive representation of the effect,  $\hat{B} + \tilde{B}$ , is naturally depicted as two columns -  $B$  and  $t$  - aligning with its original form. This approach eliminates the need for specifying  $B_{30}$  to build estimation, unlike traditional SCMs.

### 5.3 Factorization of Relation-Defined Hierarchy

Consider the relationship  $\mathcal{X} \rightarrow \mathcal{Y}$ , where  $\mathcal{X} = \langle X, t \rangle \in \mathbb{R}^{d+1}$  and  $\mathcal{Y} = \langle Y, \tau \rangle \in \mathbb{R}^{b+1}$ . Given a collection of  $n$ -level hierarchical representation functions for  $\mathcal{X}$ , denoted as  $\mathcal{F}(\vartheta) = \{f_i(\theta_i) \mid i = 1, \dots, n\}$ , we aim to define the  $n$  relationship functions, collectively referred to as  $\mathcal{G}$ , to feature  $\mathcal{Y} = \mathcal{G}(\mathcal{X})$  as  $n$ -level hierarchy. Let the  $i$ -th level relationship function be  $g_i(\mathcal{X}; \varphi_i)$  with  $\varphi_i$  denoting its parameter. Then, we have:

$$\mathcal{G}(\mathcal{X}) = \sum_{i=1}^n g_i(\mathcal{X}; \varphi_i) = \sum_{i=1}^n g_i(\Theta_i; \varphi_i) = \sum_{i=1}^n g_i(\theta_i; \Theta_1, \dots, \Theta_{i-1}, \varphi_i) = \mathcal{Y} \quad (3)$$

Therefore, the  $i$ -th level relation-defined representation of  $\mathcal{Y}$  can be expressed as  $g_i(\theta_i; \varphi_i)$  given the preceding  $(i-1)$  levels observable features of  $\mathcal{X}$  as possible attributes. In other words, the  $i$ -th level relationship can be represented as an augmented feature vector in the latent space  $\langle \theta_i, \varphi_i \rangle \in \mathbb{R}^L$ . Now, let's utilize  $\vartheta_X$  and  $\vartheta_Y$  to differentiate the collective hierarchy representations for  $\mathcal{X}$  and  $\mathcal{Y}$ , respectively. The collective relationship  $\mathcal{G}$  from  $\mathcal{X}$  to  $\mathcal{Y}$  can be represented as the latent space relationship  $\vartheta_Y = \langle \vartheta_X, \varphi \rangle$ , where  $\varphi = \{\varphi_1, \dots, \varphi_n\}$  and  $\langle \vartheta_X, \varphi \rangle$  indicates the pairwise augmentations between collection  $\vartheta_X$  and collection  $\varphi$ .

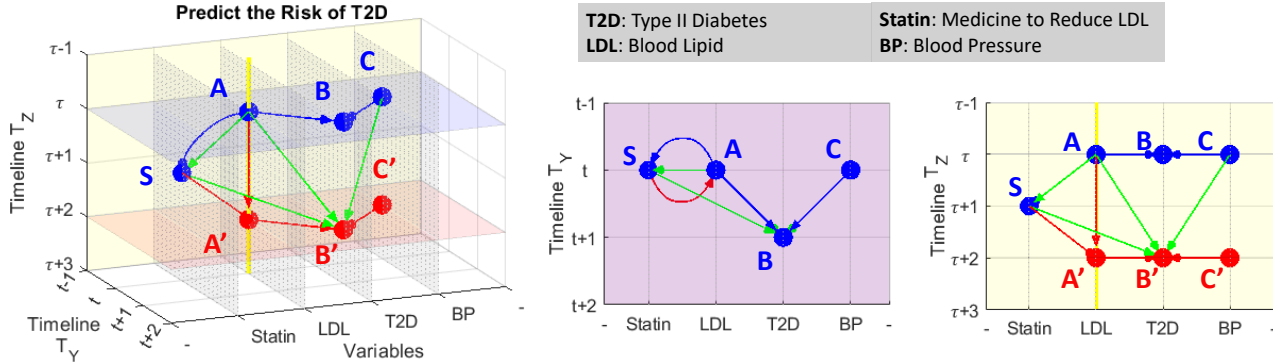


Figure 10: An example DAG in 3D observational-temporal space, where the SCM function  $B' = f(A, C, S)$  aims to evaluate Statin's medical effect on reducing the risk of T2D, with two logical timelines  $T_Y$  and  $T_Z$ . On  $T_Y$ , the step  $\Delta t$  from  $t$  to  $(t+1)$  allows  $A$  and  $C$  to fully influence  $B$ , while the step  $\Delta \tau$  on  $T_Z$ , from  $(\tau+1)$  to  $(\tau+2)$ , let medicine  $S$  completely release its effect on LDL, which is, changing  $A$  to  $A'$ .

Consider the practical scenario depicted in Figure 10. From a differential-and-integral perspective, each differentiable unit of medical effect on LDL, delivered through  $\overrightarrow{SA'}$ , immediately begins influencing T2D via  $\overrightarrow{A'B'}$ . Concurrently, the subsequent unit effect is being generated. These two processes occur simultaneously until the medication  $S$  is fully administered. Ultimately, the  $B'$  we seek to evaluate embodies the total integral influence originating from  $S$ . Put another way, the emphasis in this DAG lies not on the absolute values of  $\Delta t$  and  $\Delta \tau$ , which would represent actual time spans. Rather, it is on the meaning of the nodes, which define what  $\Delta t$  and  $\Delta \tau$  represent within this specific context.

In traditional causality theories, variables in the SCM function  $B' = f(A, C, S)$  can only signify observational aspects of these nodes. Consequently, the role of  $B'$  requires a manual specification for its temporal feature, as to determine the absolute time span for the edge  $\overrightarrow{SB'}$ . For instance, by empirical experience, the impact of  $S$  typically lasts around  $30 \pm 10$  days. Thus, the time span of  $\overrightarrow{SB'}$  is set to 30 days for the estimation of the population-level mean effect at  $B'$ .

While, how long  $\overrightarrow{SB'}$  should be set is not indeed crucial, the critical fact is that assuming a length for  $\overrightarrow{SB'}$  essentially fixes the  $\Delta t : \Delta \tau$  ratio (consider  $\overrightarrow{SB'} = \overrightarrow{SA'} + \overrightarrow{A'B'}$ ) and consequently sets the shape of triangle  $ASB'$  for the entire population. As a result, patients within the  $\pm 10$  range risk being attributed an invalid  $ASB'$ -triangle and leading to inherent temporal biases, similar to Figure 8(b)(c). More significantly, even if the mean effect at  $B'$  is accurately estimated for this particular population, the derived SCM can hardly be generalizable to all others, because the presumed  $\Delta t : \Delta \tau$  ratio may not hold true in general.

Contrarily, the proposed approach of relation-defined representation, applied in learning the edge  $\overrightarrow{SB'}$ , focuses on the role of  $B'$  as dictated by this edge, incorporating its temporal features. This obviates the need to define time spans for  $\overrightarrow{SA'}$  and  $\overrightarrow{A'B'}$ , thereby relieving us from concerning the  $\Delta t : \Delta \tau$  ratio. Within the 3D observational-temporal space, as depicted in Figure 10, we can consider any desired model individualizations for patients or generalizations for other populations as linear transformations of the green-colored subgraph.

## 6 Relation-Defined Representation Methodology

Essentially, the proposed relation-defined representation is a technique for transforming the observational-temporal entities in our cognition into features - a format that AI systems can readily understand and build models on. The inherent temporal biases underscore the observational constraints of traditional methods, while concurrently recognizing their robust ties to our existing knowledge infrastructures. As illustrated in Figure 11, we enable AI to develop generalizable models in latent feature space filled with human-unreadable representations, while harnessing its capabilities to amplify observations for bolstering the effectiveness of traditional models.

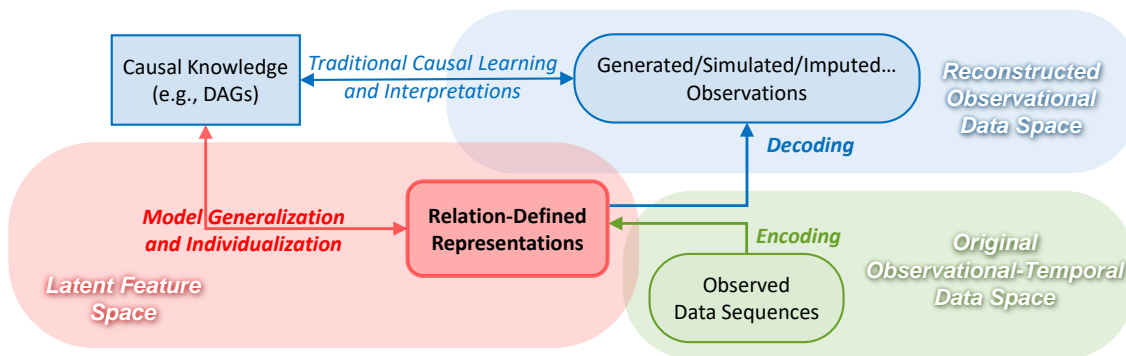


Figure 11: Framework for using *Relation-Defined Representations* to generate apt observations for traditional models, circumventing inherent temporal biases and enriching the observational modeling space.

Consider the practical example in Figure 10. Traditional methods mitigate bias in the model  $B' = f(A, C, S)$  by randomizing medication  $S$  based on  $A$ , to disrupt conditional dependence, leading to the use of selective subpopulation while discarding a significant portion. In contrast, the proposed AI approach individually models  $\overrightarrow{SB'}$  and  $\overrightarrow{AB'}$  without manual adjustments, answering counterfactual questions regarding the medicinal effect. Furthermore, these AI models can simulate de-confounded observations for traditional models, enabling comprehensive knowledge-based studies in larger comorbidity contexts.

In this section, we introduce a proposed autoencoder architecture tailored for implementing relation-defined representation learning; based on it, outline the approach for “stacking” hierarchical levels of representations within the latent space for constructing graphical models; and lastly, present a causal discovery algorithm designed to operate within this latent feature space.

## 6.1 Designing Higher-Dimensional Feature Representation Autoencoders

Autoencoders, primarily intended for dimensionality reductions Wang et al. (2016), commonly treat all variables (i.e., nodes in the Directed Acyclic Graph, DAG) as aligned observations to reduce attribute matrix dimensionality in structural modeling Luo et al. (2020). However, our focus is on modeling individual relations and “stacking” their representations to construct a DAG within the latent space  $\mathbb{R}^L$ . This demands a large dimensionality for  $\mathbb{R}^L$  to accommodate all potential hierarchical features and to sequentially build  $L$ -dimensional node representations in the DAG, hence presenting a substantial technical challenge in facilitating *high-dimensional feature representations*.

**Corollary 1.** Given a graph  $G$  and a data matrix  $\mathbf{X}$  column-augmented with all observational attributes of variables in  $G$ , along with a column for timestamps (i.e., the absolute timeline), the latent space dimensionality  $L$  must be at least as large as  $\text{rank}(\mathbf{X})$  to adequately represent  $G$ .

Corollary 1 stems from the notion that the autoencoder-learned  $\mathbb{R}^L$  is spanned by  $\mathbf{X}$ ’s top principal components, often referred to as Principal Component Analysis (PCA) Baldi & Hornik (1989); Plaut (2018); Wang et al. (2016). Hypothetically, reducing  $L$  below  $\text{rank}(\mathbf{X})$  could yield a less comprehensive but causally more significant latent space through better alignment Jain et al. (2021), although further exploration is needed. In this study, we will set aside discussions on the boundaries of dimensionality. Our experiments feature 10 variables with dimensions 1 to 5 (Table 1), and we empirically fine-tune and reduce  $L$  from 64 to 16.

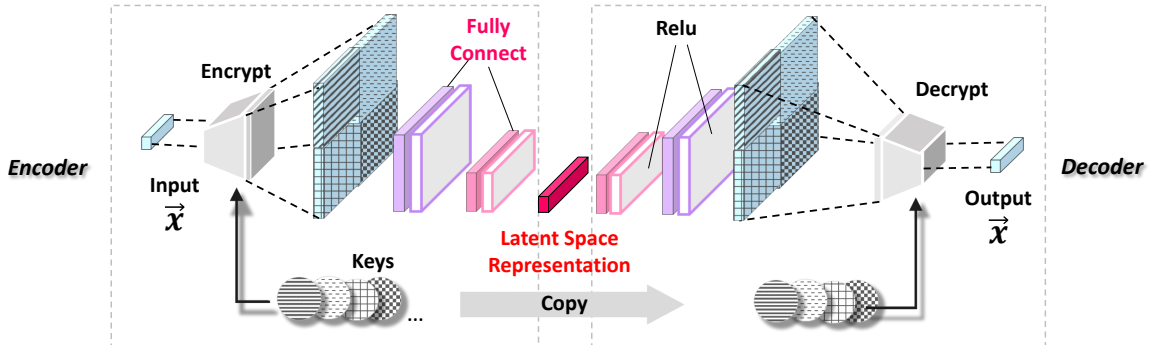


Figure 12: The proposed autoencoder architecture for *Higher-Dimensional* feature representations. The reconstructed observation  $\vec{x} \in \mathbb{R}^d$  is denoted and depicted as a vector for clarity.

Figure 12 depicts the proposed autoencoder architecture, which employs symmetrical *Encrypt* and *Decrypt* layers at the input and the output, respectively. The *Encrypt* layer acts as an amplifier, expanding the input vector  $\vec{x}$  by extracting its higher-order intrinsic features. Conversely, the *Decrypt* layer, functioning as a symmetric reducer, restores  $\vec{x}$  to its original form. To ensure reconstruction accuracy, the invertibility of these operations is naturally required. Figure 12 illustrates a *double-wise* feature expansion. In this method, each pair of *two* digits from  $\vec{x}$  is encoded into a new digit, thus capturing their association. This is accomplished using a *Key*, a set of constants created by the encoder and mirrored by the decoder for reverse decryption. The application of a double-wise expansion *Key* on  $\vec{x} \in \mathbb{R}^d$  generates a  $(d-1)(d-1)$  length vector. By utilizing multiple *Keys* and augmenting the vectors they produce,  $\vec{x}$  can be significantly extended beyond its original length  $d$ . The four differently patterned squares in Figure 12 represent the results of four distinct *Keys*. Each square visualizes a  $(d-1)(d-1)$  length vector (not suggesting 2-dimensionality), with the patterned grids indicating each *Key*’s unique “signature”. As an analogy, higher-order extensions such as *triple-wise* ones across every three digits can also be employed, by appropriately adapting the *Key* to encapsulate more intricate associations within the data.

Figure 13 illustrates the *Encrypt* and *Decrypt* functions executing a double-wise expansion. These processes transform a digit pair  $(x_i, x_j)$ ,  $i \neq j \in 1, \dots, d$ , via encryption  $f_\theta(x_i, x_j)$ , with  $\theta = (w_s, w_t)$  as the *Key* comprising two weights defining elementary functions  $s(\cdot)$  and  $t(\cdot)$ . Specifically,  $f_\theta(x_i, x_j) = x_j \otimes \exp(s(x_i)) + t(x_i)$  is applied to each digit pair, transforming  $x_j$  into a new digit  $y_j$  using  $x_i$  as a parameter. The *Decrypt*

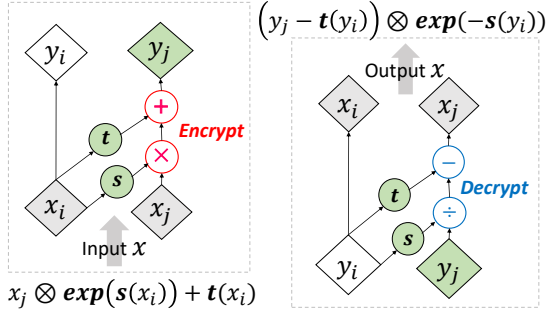


Figure 13: Encrypt (left) and Decrypt (right).

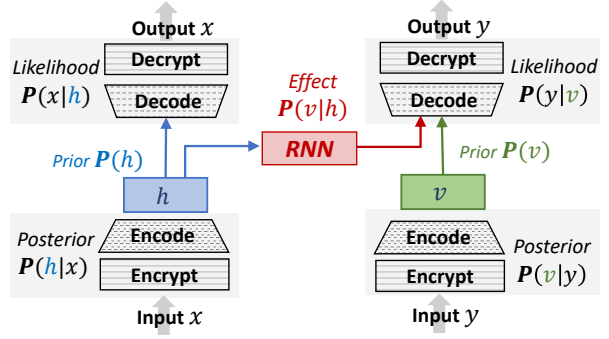


Figure 14: Architecture of Latent Effect.

layer uses the symmetric inverse function  $f_\theta^{-1}$ , defined as  $(y_j - t(y_i)) \otimes \exp(-s(y_i))$ . Importantly, this calculation sidesteps the need for  $s^{-1}$  or  $t^{-1}$ , permitting both linear and non-linear transformations. With the set of all  $f_\theta$  functions denoted as  $\mathcal{F}(X; \vartheta)$  - where  $X$  is the input variable and  $\vartheta$  comprises all parameters - the Encrypt and Decrypt layers can be represented as  $Y = \mathcal{F}(X; \vartheta)$  and  $X = \mathcal{F}^{-1}(Y; \vartheta)$ , respectively. Drawing from the seminal work of Dinh et al. Dinh et al. (2016) on invertible neural network layers, we employ bijective functions to design our autoencoder. We specifically use the double-wise extension function  $f_\theta(x_i, x_j)$ , operating on digit pairs, thus preserving reconstruction accuracy. This bijective foundation ensures our architecture's robustness and adaptability, tailoring extension levels to application requirements. The source code for Encrypt and Decrypt is provided<sup>1</sup>, along with a comprehensive experimental demo.

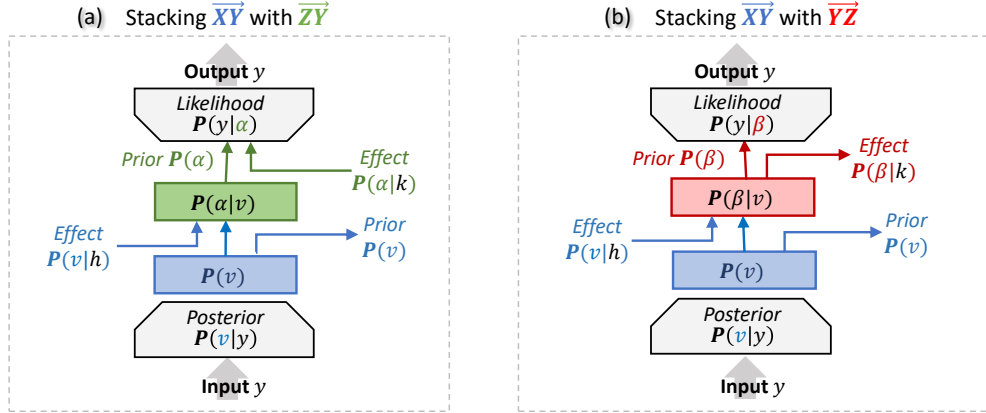


Figure 15: Architectures of the Relation-Defined Hierarchical Representation.

## 6.2 Structural Model with Hierarchical Representations

Consider a causal system comprising three variables:  $\{\mathcal{X}, \mathcal{Y}, \mathcal{Z}\}$ . For each, a corresponding representation  $\{\mathcal{H}, \mathcal{V}, \mathcal{K}\} \in \mathbb{R}^L$  is generated via independent autoencoders with the aforementioned architecture. Figure 14 portrays the process of connecting  $\mathcal{H}$  and  $\mathcal{V}$  to represent the relation  $\mathcal{X} \rightarrow \mathcal{Y}$ , while Figure 15 illustrates stacking these relations to represent the entire causal system, thereby enabling a hierarchical representation.

Assume  $x$  and  $y$  as instances of the relation  $\mathcal{X} \rightarrow \mathcal{Y}$ , with corresponding latent representations  $h$  and  $v$ . We utilize an RNN model to estimate the latent dependency  $\mathbf{P}(v|h)$  as displayed in Figure 14. The training process involves three simultaneous optimizations per iteration:

1. Optimizing encoder  $\mathbf{P}(h|x)$ , RNN model  $\mathbf{P}(v|h)$ , and decoder  $\mathbf{P}(y|v)$  to reconstruct the effect  $x \rightarrow y$ .
2. Fine-tuning encoder  $\mathbf{P}(v|y)$  and decoder  $\mathbf{P}(y|v)$  to accurately represent  $y$ .
3. Fine-tuning encoder  $\mathbf{P}(h|x)$  and decoder  $\mathbf{P}(x|h)$  to accurately represent  $x$ .

Throughout the learning,  $h$  and  $v$  values are iteratively refined to minimize their latent space distance, and the RNN functions act as a bridge to traverse this distance, thereby estimating the causal effect  $x \rightarrow y$ .

<sup>1</sup>[https://github.com/kfljia/bijective\\_crossing\\_functions/blob/main/code\\_bicross\\_extractor.py](https://github.com/kfljia/bijective_crossing_functions/blob/main/code_bicross_extractor.py)

Figure 15 presents two stacking scenarios for  $\mathcal{Y}$  in the three-variable causal system comprising  $\{\mathcal{X}, \mathcal{Y}, \mathcal{Z}\}$ , based on different causal direction settings. For the established latent edge  $\overline{XY}$ , the left-side architecture completes the  $X \rightarrow Y \leftarrow Z$  relationship, while the right-side caters to  $X \rightarrow Y \rightarrow Z$ . Stacking is achieved by adding an extra representation layer, thereby forming a hierarchical structure, enabling diverse input-output combinations (denoted as  $\mapsto$ ). For example, in the left setup,  $\mathbf{P}(v|h) \mapsto \mathbf{P}(\alpha)$  signifies the  $X \rightarrow Y$  relationship, while  $\mathbf{P}(\alpha|k)$  implies  $Z \rightarrow Y$ . Conversely, the right setup has  $\mathbf{P}(v) \mapsto P(\beta|k)$  representing  $Y \rightarrow Z$  with  $Y$  as input and  $\mathbf{P}(v|h) \mapsto P(\beta|k)$  denoting the  $X \rightarrow Y \rightarrow Z$  relationship.

Causal effects of edges can be sequentially stacked based on known causal Directed DAGs by leveraging domain knowledge. Additionally, this method can facilitate causal structure discovery in the latent space, identifying potential edges among the initial representations of the variables.

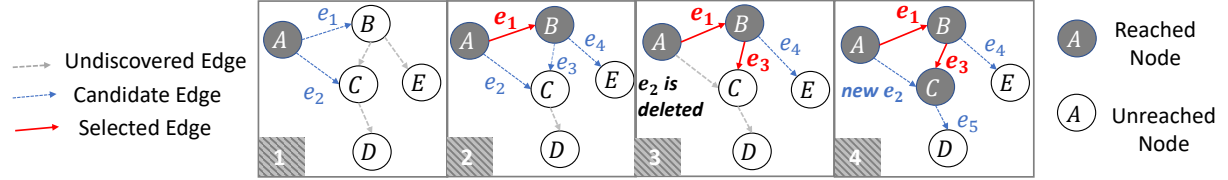


Figure 16: Example of the Latent Space Causal Discovery.

### 6.3 Causal Discovery in Latent Space

Algorithm 1 details the heuristic process of discovering causal edges among the initially established variable representations. It employs the Kullback-Leibler Divergence (KLD) as a metric to assess causal relationship strength. Specifically, KLD measures the similarity between the *RNN*'s output,  $\mathbf{P}(v|h)$ , and the prior  $\mathbf{P}(v)$ , as depicted in Figure 14. A lower KLD signifies a stronger causal relationship, given its closer alignment with the ground truth. Though Mean Squared Error (MSE) is a conventional evaluation metric, considering it may be influenced by data variances Reisach et al. (2021); Kaiser & Sipos (2021), we primarily employ KLD as the criterion and use MSE as a supplementary metric. For clarity, in the graphical context, for edge  $A \rightarrow B$ , we refer to variables  $A$  and  $B$  as the *cause node* and *result node*, respectively.

Figure 16 presents an exemplification of the causal structure discovery process within the latent space. Across four steps, two edges ( $e_1$  and  $e_3$ ) are successively selected. The selection of  $e_1$  establishes node  $B$  as the starting point for  $e_3$ . In step 3, the causal effect of  $e_2$  from  $A$  to  $C$  is deselected from the potential edges and re-evaluated. This is due to the introduction of edge  $e_3$  to  $C$ , modifying  $C$ 's existing causal conditions. As the procedure unfolds, the ultimately discovered causal structure is represented by the final DAG.

---

#### Algorithm 1: Latent Space Causal Discovery

---

**Result:** ordered edges set  $\mathbf{E} = \{e_1, \dots, e_n\}$   
 $\mathbf{E} = \{\}; N_R = \{n_0 \mid n_0 \in N, \text{Parent}(n_0) = \emptyset\};$   
**while**  $N_R \subset N$  **do**  
   $\Delta = \{\};$   
  **for**  $n \in N$  **do**  
    **for**  $p \in \text{Parent}(n)$  **do**  
      **if**  $n \notin N_R$  and  $p \in N_R$  **then**  
         $e = (p, n); \beta = \{\};$   
        **for**  $r \in N_R$  **do**  
          **if**  $r \in \text{Parent}(n)$  and  $r \neq p$  **then**  
             $\beta = \beta \cup r$   
          **end**  
        **end**  
         $\delta_e = K(\beta \cup p, n) - K(\beta, n);$   
         $\Delta = \Delta \cup \delta_e;$   
      **end**  
    **end**  
  **end**  
   $\sigma = \text{argmin}_e(\delta_e \mid \delta_e \in \Delta);$   
   $\mathbf{E} = \mathbf{E} \cup \sigma; N_R = N_R \cup n_\sigma;$   
**end**

---

$G = (N, E)$	graph $G$ consists of $N$ and $E$
$N$	the set of nodes
$E$	the set of edges
$N_R$	the set of reachable nodes
$\mathbf{E}$	the list of discovered edges
$K(\beta, n)$	KLD metric of effect $\beta \rightarrow n$
$\beta$	the cause nodes
$n$	the result node
$\delta_e$	KLD Gain of candidate edge $e$
$\Delta = \{\delta_e\}$	the set $\{\delta_e\}$ for $e$
$n, p, r$	notations of nodes
$e, \sigma$	notations of edges

## 7 Experiments

The experiments aim to validate the efficacy of the proposed *Relation-Oriented* modeling methods in: 1) creating high-dimensional feature representations using our autoencoder architecture, 2) constructing latent effects and stacking them for hierarchical representation, and 3) latent space causal structure discovery.

We employ a synthetic hydrology dataset for the experiments, a prevalent resource in hydrology. The task involves predicting streamflow based on observed environmental conditions like temperature and precipitation. By using relation-defined representation learning on this hydrology data, we aim to construct generalizable causal models across diverse watersheds. Despite similarities in hydrological schemes, differences in unmeasurable conditions such as economic developments and land use complicate direct model application. Current physical knowledge-based models, however, are often constrained by limited parameters, which restricts their flexibility in capturing complex relationships within data.

To assess the model’s robustness and generalizability, Electronic Health Records (EHR) data would have been an ideal choice, given their rich confounding relationships across multiple timelines. However, due to empirical restrictions, we lost access to the EHR data during this study. To confirm the existence of inherent temporal bias, we direct readers to the previous work Li et al. (2020). A comprehensive demonstration of the experiments in this study can be found in the provided repository<sup>2</sup>.

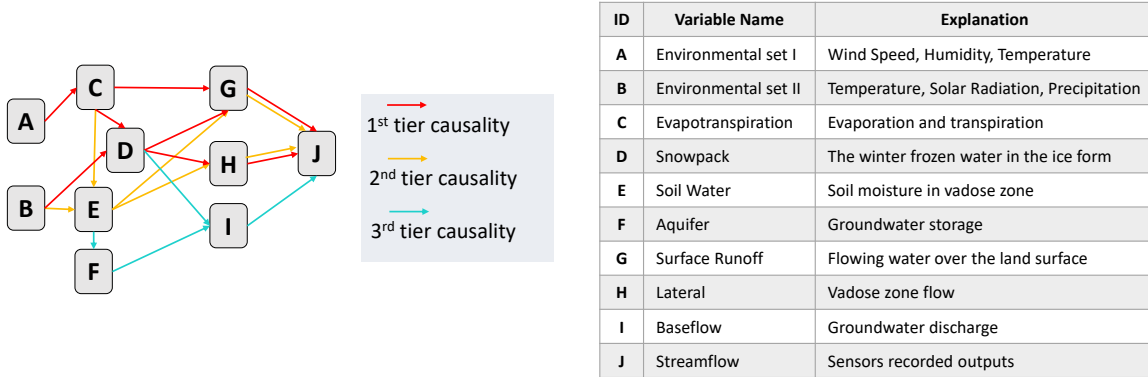


Figure 17: DAG of structured hydrology data, with tiers of routines ordered by decreasing causal strengths.

### 7.1 Hydrology Dataset

Our experiments leverage the Soil and Water Assessment Tool (SWAT), a comprehensive hydrology data simulation system rooted in physical modules. We use SWAT’s simulation of the Root River Headwater watershed in Southeast Minnesota, selecting 60 consecutive virtual years with daily updates. The performance evaluations predominantly focus on the accuracy of the autoencoder reconstructions.

In hydrology, deep learning methodologies are frequently employed Goodwell et al. (2020) to distill effective representations from time series data, with RNN models emerging as a favored choice for streamflow prediction Kratzert (2018). Figure 17 illustrates the causal DAG used by SWAT, with accompanying node descriptions. The nodes signify different hydrological routines, with the intensity of causality between them determined by their contribution to the output streamflow, denoted by various colors. The surface runoff routine (1st tier causality) plays a significant role in causing swift streamflow peaks, followed by the lateral flow routine (2nd tier causality). The baseflow dynamics (3rd tier causality) exert a more subtle influence. In our causal discovery experiments, we aim to uncover these ground truths from the observed data.

### 7.2 Higher-Dimensional Representation Reconstruction Test

As depicted in Figure 17, there are 10 nodes needing initial representation establishment. Table 1 displays the statistics of their attributes (post-normalization), and reconstruction performance using the proposed high-dimensional feature representation autoencoders. Accuracy is evaluated via root mean square error (RMSE); lower RMSE equates to higher accuracy, on both scaled (i.e., normalized) and unscaled data.

<sup>2</sup>[https://github.com/kflijia/bijective\\_crossing\\_functions.git](https://github.com/kflijia/bijective_crossing_functions.git)

Table 1: Statistics of Attributes and the Reconstruction Performances.

Variable	Dim	Mean	Std	Min	Max	Non-Zero Rate%	RMSE on Scaled	RMSE on Unscaled	BCE of Mask
A	5	1.8513	1.5496	-3.3557	7.6809	87.54	0.093	0.871	0.095
B	4	0.7687	1.1353	-3.3557	5.9710	64.52	0.076	0.678	1.132
C	2	1.0342	1.0025	0.0	6.2145	94.42	0.037	0.089	0.428
D	3	0.0458	0.2005	0.0	5.2434	11.40	0.015	0.679	0.445
E	2	3.1449	1.0000	0.0285	5.0916	100	0.058	3.343	0.643
F	4	0.3922	0.8962	0.0	8.6122	59.08	0.326	7.178	2.045
G	4	0.7180	1.1064	0.0	8.2551	47.87	0.045	0.81	1.327
H	4	0.7344	1.0193	0.0	7.6350	49.93	0.045	0.009	1.345
I	3	0.1432	0.6137	0.0	8.3880	21.66	0.035	0.009	1.672
J	1	0.0410	0.2000	0.0	7.8903	21.75	0.007	0.098	1.088

Table 2: Brief Summary of the Latent Causal Discovery Results.

Edge	A→C	B→D	C→D	C→G	D→G	G→J	D→H	H→J	B→E	E→G	E→H	C→E	E→F	F→I	I→J	D→I
KLD	7.63	8.51	10.14	11.60	27.87	5.29	25.19	15.93	37.07	39.13	39.88	46.58	53.68	45.64	17.41	75.57
Gain	7.63	8.51	1.135	11.60	2.454	5.29	25.19	0.209	37.07	-5.91	-3.29	2.677	53.68	45.64	0.028	3.384

The task poses challenges due to the exceedingly low dimensionality of the 10 variables, with a maximum of just 5 and the target node,  $J$ , possessing a single attribute. To counter this, we duplicate their columns to achieve a uniform 12-dimensionality, supplemented by the dummy variables of the 12 months, yielding a 24-dimensional autoencoder input. Through a double-wise feature extension, we generate a 576-dimensional amplified input, from which we extract a 16-dimensional representation via the encoder and decoder.

Significant challenges also arise from considerable meaningful-zero values. For example, node  $D$  (Snowpack in winter) includes numerous zeros in other seasons, closely related to node  $E$  (Soil Water) values. We address this by concurrently reconstructing non-zero indicator variables, named masks, within the autoencoder, evaluated using binary cross entropy (BCE).

Despite these challenges, the shallow RMSE values within  $[0.01, 0.09]$  suggest success, barring node  $F$  (the Aquifer). Considering that research into the physical schemes under the aquifer system is still in its infancy, it is plausible that in this synthetic dataset, node  $F$  is more representative of random noise than other nodes.

### 7.3 Latent Causal Effects Learning Test

Table 3 shows the results of the latent effect learning, organized by each result node. For convenience, the pairwise relationship performances are referred to as “pair-effect”, and the hierarchical multi-level performances as “stacking-effect”. To facilitate comparison, the baseline performances from the initial variable representation (Table 1) are also included. During latent effect estimation, each result node fulfills two roles: preserving an accurate self-representation (optimization 2), and reconstructing the effect (optimization 1). These dual roles are respectively depicted in the middle and right-hand side of Table 1.

The KLD metrics in Table 3 indicate the strength of learned causality, with a lower value signifying a stronger causal relationship. For instance, node  $J$ ’s minimal KLD values suggest a significant causal effect from nodes  $G$  (Surface Runoff),  $H$  (Lateral), and  $I$  (Baseflow). In contrast, the high KLD values imply that predicting variable  $I$  using  $D$  and  $F$  is challenging.

For nodes  $D$ ,  $E$ , and  $J$ , the stacking-effect causal strengths hover at a middle range compared to their pair-effects, suggesting a potential associative uninformative among their cause nodes. In contrast, for nodes  $G$  and  $H$ , lower stacking-effect KLDs indicate effective capture of associations by hierarchical representations. The KLD metric also unveils the most contributive cause node to the causal effect. For instance, the  $C \rightarrow G$  strength being closer to  $CDE \rightarrow G$  indicates  $C$  as the primary source of this causal effect.

Figure 18 showcases time series simulations of nodes  $J$ ,  $G$ , and  $I$ , in the same synthetic year, to provide a straightforward overview of the hierarchical representation performances. Here, blue lines represent reconstructed data, black dots the ground truth, and red lines hierarchical representations. We employ not only RMSE but also the Nash–Sutcliffe model efficiency coefficient (NSE) for accuracy evaluation, which ranges from  $-\infty$  to 1. The reconstructions closely mirror the ground truth, and as anticipated, the stacking-effect outperforms the pair-effect in Figure 18. Although node  $J$  has the best prediction, node  $I$  proves challenging. For node  $G$ , which is predicted from causes  $CDE$ ,  $C$  offers the most potent causality.

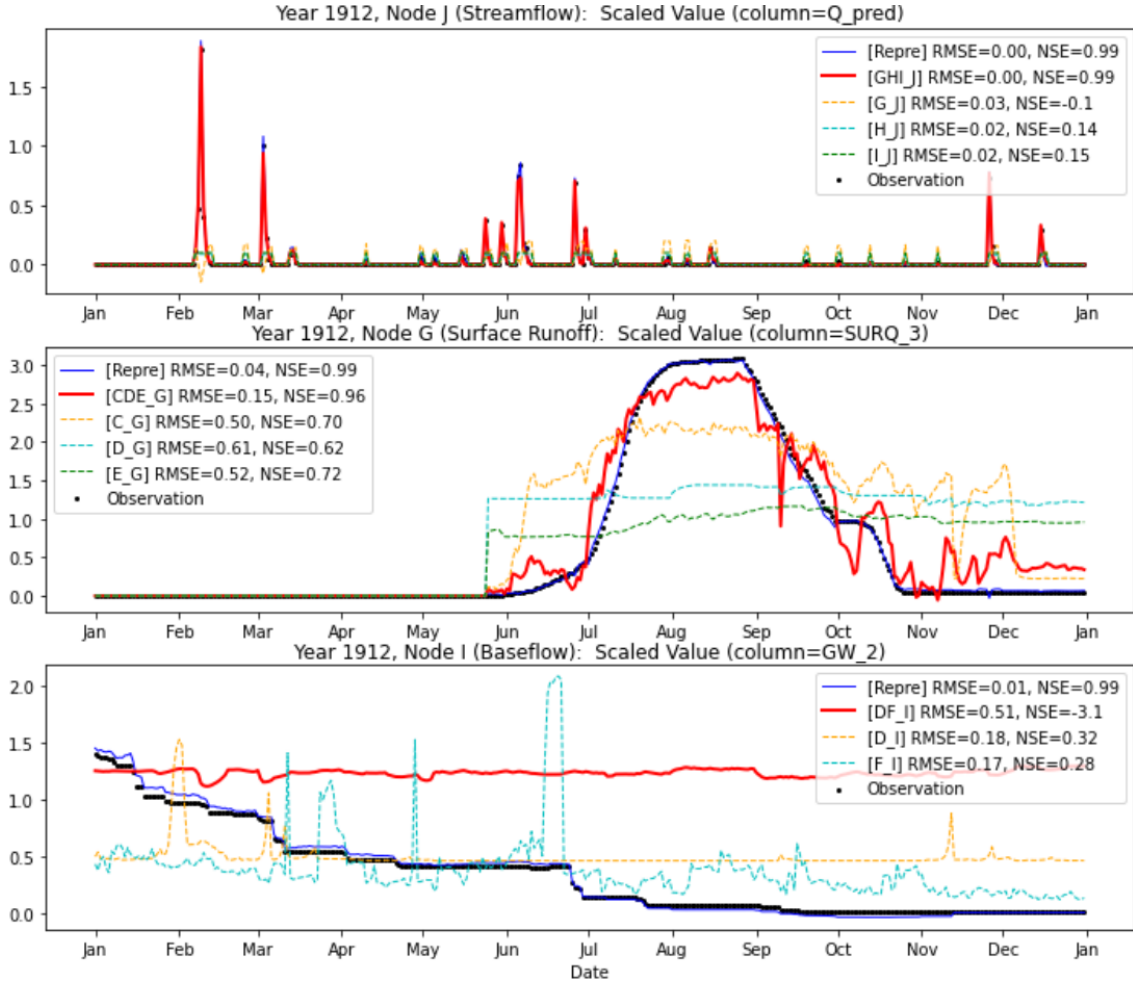


Figure 18: Time series simulation examples for the reconstruction performances' comparison.

One might observe via the demo that our experiments do not show smooth information flows along successive long causal chains. Given that RNNs are designed primarily for capturing the dynamics of causes rather than the effects, relying on them to spontaneously organize the effects' dynamical representations might prove unreliable. It underscores a significant opportunity for enhancing effectiveness by improving the architecture.

#### 7.4 Latent Space Causal Discovery Test

Table 6 shows the order of discovered edges, with the KLD values after each edge's inclusion, and respective KLD gains. Cells follow the color-coding scheme from Figure 17, representing different tiers of causal routines. For a detailed look at the causal discovery process, see 4, which presents sorted detection rounds. For comparison, we conducted a 10-fold cross-validation using the conventional FGES method; results can be found in Appendix A Table 5. The proposed method markedly outperforms the traditional FGES approach.

## 8 Conclusions

Our traditional thinking about AI often assumes that incorporating larger, more diverse datasets can lead to more substantial advances. While that indeed powers AI but also creates more significant misalignments that deviate from our knowledge and cognition. As Christian (2020) highlights, AI alignment issues extend beyond technical issues, but point to humans' "blind spots" and "unstated assumptions". We might not differentiate ourselves from AI systems based on our capacity to understand large contexts, but rather on how we perceive the individual relationship.

Table 3: Performances of Latent Causal Effect Learning via Reconstructions.

Result Node	Variable Representation (Initial)			Cause Node	Variable Representation (in Effect Learning)			Latent Causal Effect Reconstruction			
	RMSE		BCE Mask		RMSE		BCE Mask	RMSE		BCE Mask	KLD (in latent space)
	on Scaled Values	on Unscaled Values			on Scaled Values	on Unscaled Values		on Scaled Values	on Unscaled Values		
C	0.037	0.089	0.428	A	0.0295	0.0616	0.4278	0.1747	0.3334	0.4278	7.6353
D	0.015	0.679	0.445	BC	0.0350	1.0179	0.1355	0.0509	1.7059	0.1285	9.6502
				B	0.0341	1.0361	0.1693	0.0516	1.7737	0.1925	8.5147
				C	0.0331	0.9818	0.3404	0.0512	1.7265	0.3667	10.149
E	0.058	3.343	0.643	BC	0.4612	26.605	0.6427	0.7827	45.149	0.6427	39.750
				B	0.6428	37.076	0.6427	0.8209	47.353	0.6427	37.072
				C	0.5212	30.065	1.2854	0.7939	45.791	1.2854	46.587
F	0.326	7.178	2.045	E	0.4334	8.3807	3.0895	0.4509	5.9553	3.0895	53.680
G	0.045	0.81	1.327	CDE	0.0538	0.9598	0.0878	0.1719	3.5736	0.1340	8.1360
				C	0.1057	1.4219	0.1078	0.2996	4.6278	0.1362	11.601
				D	0.1773	3.6083	0.1842	0.4112	8.0841	0.2228	27.879
				E	0.1949	4.7124	0.1482	0.5564	10.852	0.1877	39.133
H	0.045	0.009	1.345	DE	0.0889	0.0099	2.5980	0.3564	0.0096	2.5980	21.905
				D	0.0878	0.0104	0.0911	0.4301	0.0095	0.0911	25.198
				E	0.1162	0.0105	0.1482	0.5168	0.0097	3.8514	39.886
I	0.035	0.009	1.672	DF	0.0600	0.0103	3.4493	0.1158	0.0099	3.4493	49.033
				D	0.1212	0.0108	3.0048	0.2073	0.0108	3.0048	75.577
				F	0.0540	0.0102	3.4493	0.0948	0.0098	3.4493	45.648
J	0.007	0.098	1.088	GHI	0.0052	0.0742	0.2593	0.0090	0.1269	0.2937	5.5300
				G	0.0077	0.1085	0.4009	0.0099	0.1390	0.4375	5.2924
				H	0.0159	0.2239	0.4584	0.0393	0.5520	0.4938	15.930
				I	0.0308	0.4328	0.3818	0.0397	0.5564	0.3954	17.410

This study advocates for a “*Relation-Oriented*” modeling principle, which could disrupt our prevalent *Observation-Oriented* modeling convention and align more closely with the relation-centric nature of human comprehension. To be specific, the knowledge nodes we construct in our cognition, are motivated by, and indexed through, relationships that confer them specific meanings under our comprehension context, rather than solely reflecting observations. Through relations, our understanding can surpass observational limitations, spanning: **1)** hyper-dimensions that encompass unobservable knowledge hierarchies, and **2)** temporal spaces where we store dynamic events, governed by multiple logical timelines.

Additionally, this study presents a feasible *Relation-Oriented* modeling technique, extracting relation-defined representations from observations, to instantiate the knowledge nodes in our understanding. AI alignment is never a question with a simple answer, but calls for our interdisciplinary efforts Christian (2020). Through this work, we aim to pave the way toward truly authentic AI and lay the groundwork for future progress.

## Acknowledgements

I want to extend my heartfelt thanks to my friend, Dr. Gao Qiman, the lone companion willing to engage in profound philosophical discussions with me, and who has provided invaluable advice. Furthermore, I express my gratitude to GPT-4 for its crucial aid in improving my English writing.

Jia Li

---

## References

- Pierre Baldi and Kurt Hornik. Neural networks and principal component analysis: Learning from examples without local minima. *Neural networks*, 2(1):53–58, 1989.
- Christopher P Burgess, Irina Higgins, Arka Pal, Loic Matthey, Nick Watters, Guillaume Desjardins, and Alexander Lerchner. Understanding disentangling in vae. *arXiv preprint arXiv:1804.03599*, 2018.
- Brian Christian. *The alignment problem: Machine learning and human values*. 2020.
- A Philip Dawid. Conditional independence in statistical theory. *Journal of the Royal Statistical Society: Series B (Methodological)*, 41(1):1–15, 1979.
- Laurent Dinh, Jascha Sohl-Dickstein, and Samy Bengio. Density estimation using real nvp. *arXiv:1605.08803*, 2016.
- Felix Elwert. Graphical causal models. *Handbook of causal analysis for social research*, pp. 245–273, 2013.
- Dan Geiger and Judea Pearl. Logical and algorithmic properties of conditional independence and graphical models. *The annals of statistics*, 21(4):2001–2021, 1993.
- Clark Glymour, Kun Zhang, and Peter Spirtes. Review of causal discovery methods based on graphical models. *Frontiers in genetics*, 10:524, 2019.
- Allison E Goodwell, Peishi Jiang, Benjamin L Ruddell, and Praveen Kumar. Debates—does information theory provide a new paradigm for earth science? causality, interaction, and feedback. *Water Resources Research*, 56(2):e2019WR024940, 2020.
- Yimin Huang and Marco Valtorta. Pearl’s calculus of intervention is complete. *arXiv preprint arXiv:1206.6831*, 2012.
- Aapo Hyvärinen, Kun Zhang, Shohei Shimizu, and Patrik O Hoyer. Estimation of a structural vector autoregression model using non-gaussianity. *Journal of Machine Learning Research*, 11(5), 2010.
- Saachi Jain, Adityanarayanan Radhakrishnan, and Caroline Uhler. A mechanism for producing aligned latent spaces with autoencoders. *arXiv preprint arXiv:2106.15456*, 2021.
- Marcus Kaiser and Maksim Sipos. Unsuitability of notears for causal graph discovery. *arXiv:2104.05441*, 2021.
- Frederik et. al Kratzert. Rainfall–runoff modelling using lstm networks. *Hydrology and Earth System Sciences*, 22(11):6005–6022, 2018.
- Sébastien Lachapelle, Philippe Brouillard, Tristan Deleu, and Simon Lacoste-Julien. Gradient-based neural dag learning. *arXiv preprint arXiv:1906.02226*, 2019.
- Jia Li, Xiaowei Jia, Haoyu Yang, Vipin Kumar, Michael Steinbach, and Gyorgy Simon. Teaching deep learning causal effects improves predictive performance. *arXiv preprint arXiv:2011.05466*, 2020.
- Yunan Luo, Jian Peng, and Jianzhu Ma. When causal inference meets deep learning. *Nature Machine Intelligence*, 2(8):426–427, 2020.
- Jianzhu et. al Ma. Using deep learning to model the hierarchical structure and function of a cell. *Nature methods*, 15(4):290–298, 2018.
- Mariusz Maziarz. A review of the granger-causality fallacy. *The journal of philosophical economics: Reflections on economic and social issues*, 8(2):86–105, 2015.

- 
- Mohammed Ombadi, Phu Nguyen, Soroosh Sorooshian, and Kuo-lin Hsu. Evaluation of methods for causal discovery in hydrometeorological systems. *Water Resources Research*, 56(7):e2020WR027251, 2020.
- Judea Pearl. Causal inference in statistics: An overview. 2009.
- Judea Pearl. The do-calculus revisited. *arXiv preprint arXiv:1210.4852*, 2012.
- Judea Pearl et al. Models, reasoning and inference. *Cambridge, UK: CambridgeUniversityPress*, 19(2), 2000.
- Jonas Peters, Joris M Mooij, Dominik Janzing, and Bernhard Schölkopf. Causal discovery with continuous additive noise models. 2014.
- Jonas Peters, Dominik Janzing, and Bernhard Schölkopf. *Elements of causal inference: foundations and learning algorithms*. The MIT Press, 2017.
- David Pitt. Mental Representation. In Edward N. Zalta and Uri Nodelman (eds.), *The Stanford Encyclopedia of Philosophy*. Metaphysics Research Lab, Stanford University, Fall 2022 edition, 2022.
- Elad Plaut. From principal subspaces to principal components with linear autoencoders. *arXiv:1804.10253*, 2018.
- Alexander G Reisach, Christof Seiler, and Sebastian Weichwald. Beware of the simulated dag! varsortability in additive noise models. *arXiv preprint arXiv:2102.13647*, 2021.
- Richard Scheines. An introduction to causal inference. 1997.
- Bernhard Schölkopf, Francesco Locatello, Stefan Bauer, Nan Rosemary Ke, Nal Kalchbrenner, Anirudh Goyal, and Yoshua Bengio. Toward causal representation learning. *IEEE*, 109(5):612–634, 2021.
- Richard S Sutton and Andrew G Barto. *Reinforcement learning: An introduction*. MIT press, 2018.
- Matej Vuković and Stefan Thalmann. Causal discovery in manufacturing: A structured literature review. *Journal of Manufacturing and Materials Processing*, 6(1):10, 2022.
- Yasi Wang, Hongxun Yao, and Sicheng Zhao. Auto-encoder based dimensionality reduction. 184:232–242, 2016.
- Christopher J Wood and Robert W Spekkens. The lesson of causal discovery algorithms for quantum correlations: Causal explanations of bell-inequality violations require fine-tuning. *New Journal of Physics*, 17(3):033002, 2015.
- Haoyan Xu, Yida Huang, Ziheng Duan, Jie Feng, and Pengyu Song. Multivariate time series forecasting based on causal inference with transfer entropy and graph neural network. *arXiv:2005.01185*, 2020.
- Xun Zheng, Bryon Aragam, Pradeep K Ravikumar, and Eric P Xing. Dags with no tears: Continuous optimization for structure learning. *Advances in neural information processing systems*, 31, 2018.
- Xun Zheng, Chen Dan, Bryon Aragam, Pradeep Ravikumar, and Eric Xing. Learning sparse nonparametric dags. In *International Conference on Artificial Intelligence and Statistics*, pp. 3414–3425. PMLR, 2020.

## A Appendix: Complete Experimental Results of Causal Discovery

Table 4: The Complete Results of Heuristic Causal Discovery in latent space. Each row stands for a round of detection, with ‘#’ identifying the round number, and all candidate edges are listed with their KLD gains as below. 1) Green cells: the newly detected edges. 2) Red cells: the selected edge. 3) Blue cells: the trimmed edges accordingly.

# 1	A → C	A → D	A → E	A → F	B → C	B → D	B → E	B → F
	7.6354	19.7407	60.1876	119.7730	8.4753	8.5147	65.9335	132.7717
# 2	A → D	A → E	A → F	B → D	B → E	B → F	C → D	C → E
	19.7407	60.1876	119.7730	8.5147	65.9335	132.7717	10.1490	46.5876
# 3	A → D	A → E	A → F	B → E	B → F	C → D	C → E	C → F
	9.7357	60.1876	119.7730	65.9335	132.7717	1.1355	46.5876	111.2978
# 4	A → E	A → F	B → E	B → F	C → E	C → F	C → G	C → H
	60.1876	119.7730	65.9335	132.7717	46.5876	111.2978	11.6012	39.2361
# 5	A → E	A → F	B → E	B → F	C → E	C → F	C → H	C → I
	60.1876	119.7730	65.9335	132.7717	46.5876	111.2978	39.2361	95.1564
# 6	A → E	A → F	B → E	B → F	C → E	C → F	C → H	C → I
	60.1876	119.7730	65.9335	132.7717	46.5876	111.2978	39.2361	95.1564
# 7	A → E	A → F	B → E	B → F	C → E	C → F	C → H	C → I
	60.1876	119.7730	65.9335	132.7717	46.5876	111.2978	39.2361	95.1564
# 8	A → E	A → F	B → E	B → F	C → E	C → F	C → I	D → E
	60.1876	119.7730	65.9335	132.7717	46.5876	111.2978	95.1564	63.7348
# 9	A → E	A → F	B → E	B → F	C → E	C → F	C → I	D → E
	60.1876	119.7730	65.9335	132.7717	46.5876	111.2978	95.1564	63.7348
# 10	A → F	B → E	B → F	C → F	C → I	D → E	D → F	D → G
	119.7730	-6.8372	132.7717	111.2978	95.1564	17.0407	123.3203	27.8798
# 11	A → F	B → F	C → F	C → I	D → F	D → G	E → F	E → G
	119.7730	132.7717	111.2978	95.1564	123.3203	53.6806	53.6806	5.2924
# 12	A → F	B → F	C → F	C → I	D → F	D → G	E → H	E → I
	119.7730	132.7717	111.2978	95.1564	123.3203	53.6806	-3.2931	110.2558
# 13	A → F	B → F	C → F	C → I	D → F	D → G	E → H	E → I
	119.7730	132.7717	111.2978	95.1564	123.3203	53.6806	-3.2931	110.2558
# 14	C → I	D → I	E → I	F → I	F → J	F → K	F → L	F → M
	95.1564	75.5775	110.2558	45.6490	0.0284	0.0284	0.0284	0.0284
# 15	C → I	D → I	E → I	F → I	F → J	F → K	F → L	F → M
	15.0222	3.3845	0.0284	0.0284	0.0284	0.0284	0.0284	0.0284
# 16	C → I	D → I	E → I	F → I	F → J	F → K	F → L	F → M
	15.0222	3.3845	0.0284	0.0284	0.0284	0.0284	0.0284	0.0284

Table 5: Average performance of 10-Fold FGES (Fast Greedy Equivalence Search) causal discovery, with the prior knowledge that each node can only cause the other nodes with the same or greater depth with it. An edge means connecting two attributes from two different nodes, respectively. Thus, the number of possible edges between two nodes is the multiplication of the numbers of their attributes, i.e., the lengths of their data vectors. (All experiments are performed with 6 different Independent-Test kernels, including chi-square-test, d-sep-test, disc-bic-test, fisher-z-test, myplr-test. But their results turn out to be identical.)

Cause Node	A	B	C			D			E	F	G	H	I			
True Causation	A → C	B → D	B → E	C → D	C → E	C → G	D → G	D → H	D → I	E → F	E → G	E → H	F → I	G → J	H → J	I → J
Number of Edges	16	24	16	6	4	8	12	12	9	8	8	8	12	4	4	3
Probability of Missing	0.038889	0.125	0.125	0.062	0.06875	0.039286	0.069048	0.2	0.142857	0.3	0.003571	0.2	0.142857	0.0	0.072727	0.030303
Wrong Causation Times of Wrongly Discovered				C → F				D → E	D → F				F → G	G → H	G → I	H → I
				5.6				1.2	0.8				5.0	8.2	3.0	2.8

Table 6: Brief Results of the Heuristic Causal Discovery in latent space, identical with Table 3 in the paper body, for better comparison to the traditional FGES methods results on this page.

The edges are arranged in detected order (from left to right) and their measured causal strengths in each step are shown below correspondingly. Causal strength is measured by KLD values (less is stronger). Each round of detection is pursuing the least KLD gain globally. All evaluations are in 4-Fold validation average values. Different colors represent the ground truth causality strength tiers (referred to the Figure 10 in the paper body).

Causation	A → C	B → D	C → D	C → G	D → G	G → J	D → H	H → J	C → E	B → E	E → G	E → H	E → F	F → I	I → J	D → I
KLD	7.63	8.51	10.14	11.60	27.87	5.29	25.19	15.93	46.58	65.93	39.13	39.88	53.68	45.64	17.41	75.57
Gain	7.63	8.51	1.135	11.60	2.454	5.29	25.19	0.209	46.58	-6.84	-5.91	-3.29	53.68	45.64	0.028	3.384